Metastatic infiltration of nervous tissue and periosteal nerve sprouting in multiple myeloma induced bone pain

Abbreviated title: Myeloma-induced bone pain.

Marta Diaz-delCastillo[1,2,3,4,5], Oana Palasca[6], Tim T. Nemler[1], Didde M Thygesen[1], Norma A Chávez-Saldaña[7], Juan A Vázquez-Mora[7], Lizeth Y Ponce Gomez[7], Lars Juhl Jensen[6], Holly Evans[3,4], Rebecca E. Andrews[3,4,5], Aritri Mandal[3,4,5], David Neves[8], Patrick Mehlen[8,9], James P Caruso[10,11], Patrick M. Dougherty[12], Theodore J Price[10], Andrew Chantry[3,4,5], Michelle A Lawson[3,4], Thomas L. Andersen[2,13,14], Juan M Jimenez-Andrade[7], Anne-Marie Heegaard[1]

[1]Department of Drug Design and Pharmacology, University of Copenhagen, 2100 Copenhagen, Denmark. [2]Department of Forensic Medicine, Århus University, 8870 Århus, Denmark. [3]Department of Oncology & Metabolism, University of Sheffield, S10 2RX Sheffield, UK. [4]Mellanby Centre for Bone Research, University of Sheffield, S10 2RX Sheffield, UK. [5]Sheffield Teaching Hospitals, S10 2JF Sheffield, UK. [6]Novo Nordisk Foundation Center for Protein Research, University of Copenhagen, 2200 Copenhagen, Denmark. [7]Unidad Académica Multidisciplinaria Reynosa Aztlan, Autonomic University of Tamaulipas, 88740 Reynosa, Mexico [8]NETRIS Pharma, 69008 Lyon, France [9]Apoptosis, Cancer and Development Laboratory- Equipe labellisée 'La Ligue', LabEx DEVweCAN, Centre de Recherche en Cancérologie de Lyon,69008 Lyon, France. [10]University of Texas at Dallas, Department of Neuroscience and Center for Advanced Pain, 75080 Texas, USA. [11]Department of Neurological Surgery, University of Texas Southwestern Medical Center, Dallas, 75390 Texas, USA. [12]Department of Pain Medicine, Division of Anesthesiology; MD Anderson Cancer Center, Houston, 77030 Texas, USA. [13]Department of Clinical Cell Biology, University of Southern Denmark, 5230 Odense, Denmark. [14]Department of Clinical Pathology, Odense University Hospital, 5000 Odense, Denmark.

Corresponding author:

Marta Diaz-delCastillo, PhD, Post-doctoral researcher

E-mail addresses: marta@forens.au.dk. Phone: +45 71832607

Institute for Forensic Medicine, Department of Forensic Medicine

Palle Juul-Jensens Boulevard 99, DK-8200, Aarhus N, Denmark.

Number of pages: 36

Number of figures: 7

Number of words in abstract: 199

Number of words in introduction: 367

Number of words in discussion: 1451

Conflicts of interest:

The authors declare no competing financial interests

Abstract:

Multiple myeloma (MM) is a neoplasia of B plasma cells that often induces bone pain. However, the mechanisms underlying myeloma-induced bone pain (MIBP) are mostly unknown. Using a syngeneic MM mouse model, we show that periosteal nerve sprouting of calcitonin-gene related protein ($CGRP^+$) and growth associated protein 43 ($GAP43^+$) fibres occurs concurrent to the onset of nociception and its blockade provides transient pain relief. MM patient samples also showed increased periosteal innervation. Mechanistically, we investigated MM induced gene expression changes in the dorsal root ganglia (DRG) innervating the MM-bearing bone and found alterations in pathways associated with cell cycle, immune response and neuronal signalling. The MM transcriptional signature was consistent with metastatic MM infiltration to the DRG, a never-before described feature of the disease that we further demonstrated histologically. In the DRG, MM cells caused loss of vascularization and neuronal injury, which may contribute to late-stage MIBP. Interestingly, the transcriptional signature of a MM patient was consistent with MM cell infiltration to the DRG. Overall, our results suggest that MM induces a plethora of peripheral nervous system alterations that may contribute to the failure of current analgesics and suggest neuroprotective drugs as appropriate strategies to treat early onset MIBP.

Significance statement:

Multiple myeloma induces periosteal nerve sprouting and metastasizes to the dorsal root ganglia, damaging blood vessels and causing transcriptional alterations that may mediate myeloma-induced bone pain.

Introduction

Multiple myeloma (MM) is an incurable malignant bone marrow disorder characterized by abnormal immunoglobulemia along with the development of osteolytic bone lesions, hypercalcaemia, renal impairment and anaemia (1). Research into the mechanisms of MM has grown exponentially over the last few decades, leading to the introduction of novel therapies such as autologous stem cell transplantation, proteasome inhibitors and immunomodulators as first-line treatment for the disease, which altogether have doubled the median survival time of MM patients (2, 3). As research attempts to convert MM into a chronic condition, improving the patients´ quality of life becomes crucial. In a 2016 systematic review of symptom prevalence across MM patients, pain and fatigue were listed as the most common complaints with over 70% of patients reporting pain, which was described as severe in over 40% (4). Moreover, a profound disconnect exists between the patients´ self-reported pain experience and their physicians´ estimation, with recent research suggesting that almost half of attending clinicians underestimate the severity of bone pain in this patient population (5).

Today, pain management in MM patients includes disease-modifying agents targeted to reducing bone disease (i.e. bisphosphonates, denosumab, radiotherapy) and opioids, often in combination with a corticosteroid as adjuvant (6, 7). On top of well-known side effects of opioids, such as constipation, development of tolerance and risk of addiction, their effect on breakthrough pain, a common occurrence in bone cancer, is limited (8). Thus, there is an evident need to unravel the pathogenesis of bone pain in MM, which may lead to mechanism-based strategies to alleviate symptom burden and improve quality of life in a growing patient population.

In a previous study, we established a local, immunocompetent mouse model of myeloma-induced bone pain (MIBP) through intrafemoral transplantation of 5TGM1-GFP cells in C57BL/KaLwRijHsd mice (9). In this model, we observed the development of pain-like behaviours over time, which were only partially reversed by systemic antiresorptive therapy; moreover, our study showed profound bone marrow denervation at the terminal stages of the model. Here, we investigate central and peripheral dysregulations driving the onset and maintenance of MIBP.

Results

Intrafemoral inoculation of 5TGM1-GFP cells induces nociception

To understand the time course of neuronal changes leading to MIBP and the mechanisms involved, we conducted a time course study where C57BL/KaLwRijHsd mice were transplanted with 5TGM1-GFP MM cells or vehicle into the medullary cavity of the femur and their pain-like behaviours were assayed over time (Figure 1A). A subset of animals was then euthanized on post-surgical day 17 (sham^{D17} and MM^{D17}), prior to development of pain-like behaviours (Figure 1B, C) and another on post-surgical day 24 (sham^{D24} and MM^{D24}), upon the onset of nociception, as measured by limb use and burrowing tests (Figure 1D, 1E). These behavioural deficits were not a result of impaired motor function (Supplementary Fig S1). Disease development was confirmed by paraproteinemia in both animal cohorts (Figure 1G, I). MM^{D24} mice, but not MM^{D17} mice, also presented splenomegaly (Figure 1F, H), a common feature of 5T MM animal models.

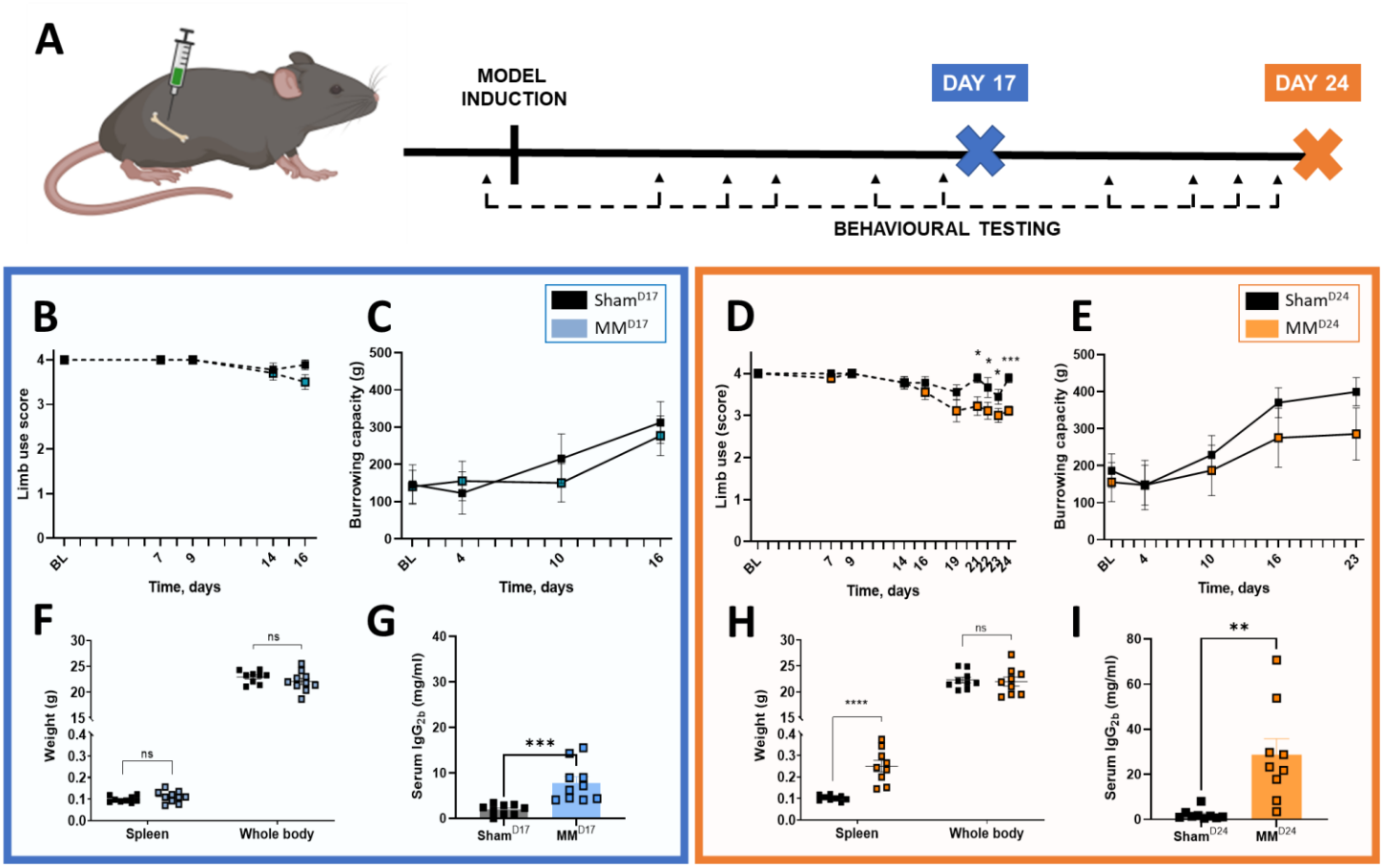

Figure 1. Intrafemoral 5TGM1-GFP cell inoculation in C57BL/KaLwRijHsd mice induces MM disease and pain-like behaviours over time. (A) C57BL/KaLwRijHsd mice were intrafemorally inoculated with 5TMG1-GFP cells or vehicle, their pain-like behaviours were assessed over time, and mice were euthanized on post-surgical day 17 or 24. (B, D) Limb use scores were measured over time. * $p<0.05$; *** $p<0.001$ by Friedman´s two-way test followed by Wilcoxon´s two-sample test. (C, E) Burrowing capacity measured over time. (F, H) End-point spleen and whole-body weight. $t(14)=5.98$, $p<0.0001$ by unpaired, two-tailed Student´s *t*-test. (G, I) Endpoint serum levels of IgG_{2b} paraprotein. D17: $t(17)=4.068$, $p=0.0008$; D24: $t(16)=3.70$, $p=0.0019$ by unpaired, two-tailed Student´s *t*-test. BL= Baseline. Sham n=8-9; MM n=8-10.

5TGM1-GFP cells induce a time-dependent pattern of osteolytic lesion development

In previous experiments we observed a partial analgesic effect of bisphosphonates in the localized 5TGM1 model (10), suggesting that MIBP may correlate with osteolysis. Similarly, a plethora of clinical studies have shown that, like in animal models, the clinical analgesic effect of bisphosphonates in MIBP is arguable (11). To examine whether the pattern of myeloma-induced osteolysis correlates with the onset of nociception in this model, we performed µCT analyses of the ipsilateral femoral metaphysis of sham and myeloma-bearing bones. We observed that MM^{D24} present a significant increase in cortical lesion area/bone surface (BS), compared with $sham^{D24}$ (Figure 2I, J). In contrast, the lesion area/BS of MM^{D17} remained unchanged, indicating that osteolytic cortical damage develops concurrently to the onset of nociception (Figure 2A, B). Furthermore, our analyses revealed unchanged cortical bone volume in both MM^{D17} and MM^{D24} femurs (Figure 2C, K).

Next, we evaluated the effect of 5TGM1 cell inoculation in trabecular bone before and during nociception. Densitometric analyses of MM^{D17} trabecular bone revealed a significant decrease in trabecular thickness (Tb.Th) and number (Tb.N), along with increased trabecular spacing (Tb.S), indicating trabecular bone loss prior to the development of nociception (Figure 2F-H). Moreover, MM^{D17} femurs presented decreased trabecular bone volume per total volume (BV/TV) and increased

relative bone surface (BS/BV), compared with sham^{D17} (Figure 2D, E). As expected, MM^{D24} femurs presented a similar pattern of trabecular osteolysis, measured as significantly decreased BV/TV and Tb.N., along with increased Tb.Sp (Figure 2 L-P).

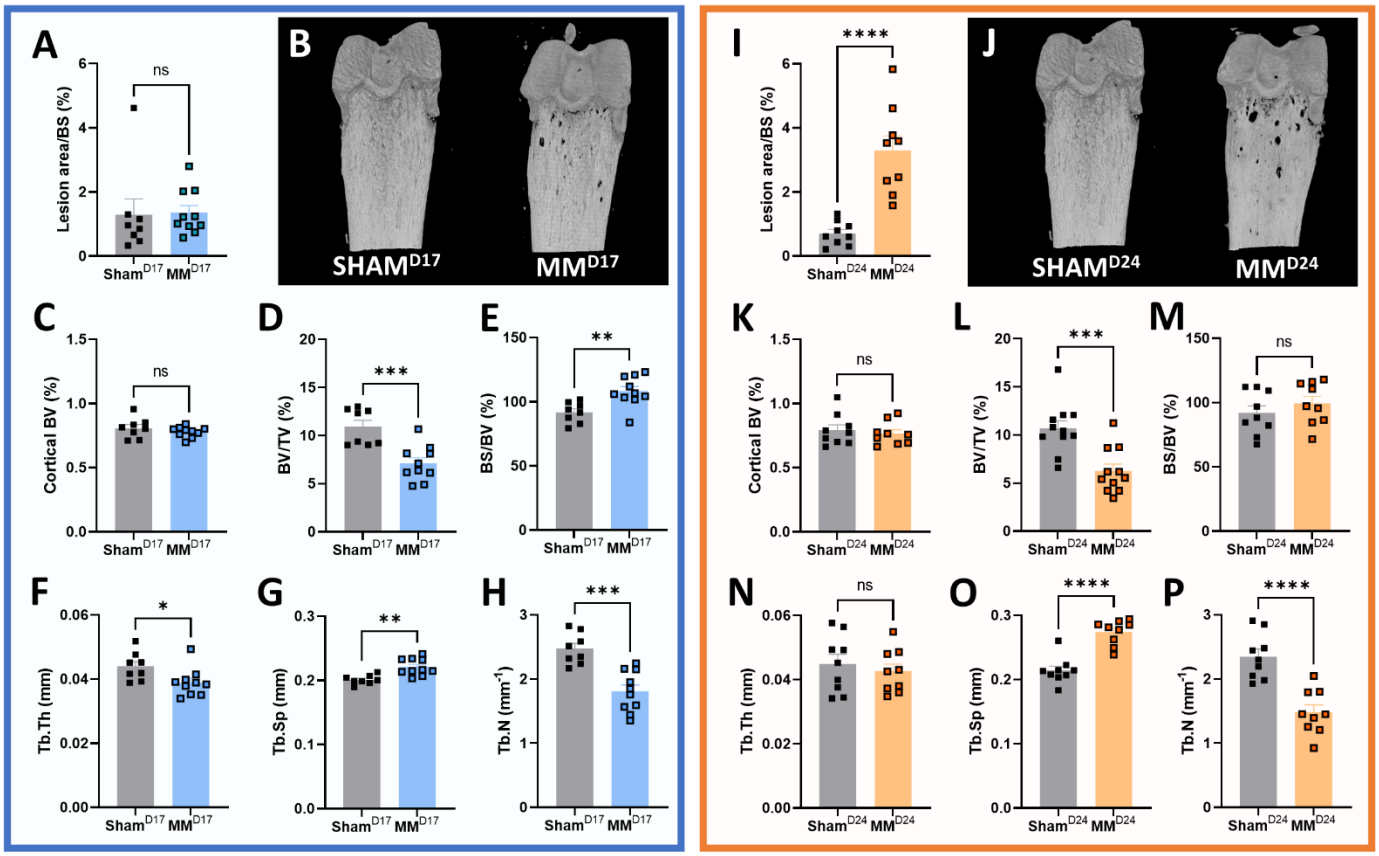

Figure 2. Temporal evolution of myeloma-induced bone disease in 5TGM1-GFP bearing femurs. (A, I) Percentage of lesion area per bone surface (lesion area/BS). ****p<0.0001 by unpaired, two-tailed Student´s t-test. (B, J) Representative µCT reconstruction images of sham and MM femurs at different time-points. (C, K) Percentage of cortical bone volume (BV). (D, L) Percentage of bone volume per total volume (BV/TV). ***p<0.001 by unpaired, two-tailed Student´s t-test. (E, M) Percentage of bone surface per bone volume (BS/BV). **p<0.01 by unpaired, two-tailed Student´s *t*-test. (F, N) Percentage of trabecular thickness (Tb.Th). *p<0.05 by unpaired, two-tailed Student´s t-test. (G, O) Percentage of trabecular separation (Tb.Sp). **p<0.01; ****p<0.0001 by unpaired, two-tailed Student´s t-test. (H, P) Percentage of trabecular number (Tb.N). ***p<0.001; ****p<0.0001 by unpaired, two-tailed Student´s t-test. Sham n=8-9; MM n=9-10.

Multiple myeloma induces periosteal nerve sprouting concomitant to nociception

Our previous studies revealed that 5TGM1 inoculation induced complete bone marrow denervation at the end stages of the model, leading us to speculate that tumour-induced nerve injury contributes to MIBP. To further evaluate the temporal effect of 5TGM1 cell inoculation on the bone marrow microenvironment, we performed immunohistological analyses of sensory (calcitonin-gene related peptide, $CGRP^+$) and sympathetic (tyrosine hydroxylase, TH^+) nerve fibres. We observed that already in MM^{D17} femurs, TH^+ and $CGRP^+$ fibres were not detectable in the bone marrow, which had been colonized by 5TGM1-GFP^+ cells (Figure 3E, G), suggesting that tumour-induced nerve injury in the bone marrow is not a main player in MIBP. To confirm that the absence of marrow innervation was not a result of technical difficulties, we identified both TH^+ and $CGRP^+$ nerve fibres in bones of the $sham^{D17}$ mice (Figure 3B-D) and in the periosteum of MM^{D17} (Fig 3F, H).

We next sought to examine the effect of intrafemoral 5TGM1-GFP inoculation on periosteal innervation. The periosteum is the bone compartment with the highest nerve density (12, 13) and alterations to periosteal nerve fibre innervation have been described as a feature of bone pain (14, 15), including cancer-induced bone pain (16, 17). Importantly, we found a significant increase in the density of $CGRP^+$ fibres innervating the periosteum of MM^{D24} mice at the onset of nociception, compared with $sham^{D24}$ (Figure 3I, M, P), which was not present at earlier stages (Figure 3K, O). Similarly, the growth associated protein-43 (GAP-34) marker of axonal growth and regeneration demonstrated significant periosteal sprouting in the later stage of MM development (Figure 3L, N, S). Periosteal nerve sprouting was present in over half of the 5TGM1-GFP inoculated mice at the onset of nociception, but never at earlier stages (Figure 3O, R, Q, T); this is consistent with the escape of 5TGM1-GFP^+ cells to the periosteum observed in MM^{D24} femurs that was not present on MM^{D17}. Altogether, our data suggests that MM cells induce cortical osteolytic lesions that allow escape to the periosteum, where they may promote periosteal nerve sprouting and contribute to the development of nociception.

To investigate the human relevance of our findings, we next examined whether periosteal infiltration of MM cells in patients is associated with nerve sprouting. In formalin-fixed, paraffin-embedded trephine iliac crest bone biopsies from 13 newly diagnosed MM (NDMM) patients, we performed a multiplex immunostaining for $CD138^+$ MM cells, $CD34^+$ blood vessels and the pan-neuronal marker PGP9.5 (Figure 3U). Our quantification showed that the median periosteal nerve density in NDMM patients was 3.736 profiles/mm^2, ranging from 0 to 82.869 profiles/mm^2 (Figure 3V); this is in contrast with reports of periosteal nerve density in non-cancerous patients showing a median of 0.077 profiles/mm^2 (range: 0.02-0.68 profiles/mm^2) (18). Moreover, we found a significant increase in periosteal nerve density in NDMM displaying periosteal infiltration of $CD138^+$ cells (Fig 3W), suggesting a direct role for MM cells in promoting nerve sprouting. Periosteal nerve density in NDMM patients was positively correlated with age (Figure 3X; R^2=0.33; $p<0.05$) but independent of tumour burden, which was assessed as percentage bone marrow clonality (Figure 3Y) and paraproteinemia (Figure 3Z). Moreover, periosteal nerve density was independent of sex and IgG type (data not shown). This is, to our knowledge, the first evidence of MM-induced alterations to bone innervation in MM patients and altogether our data suggest that periosteal nerve sprouting may play a role in MIBP.

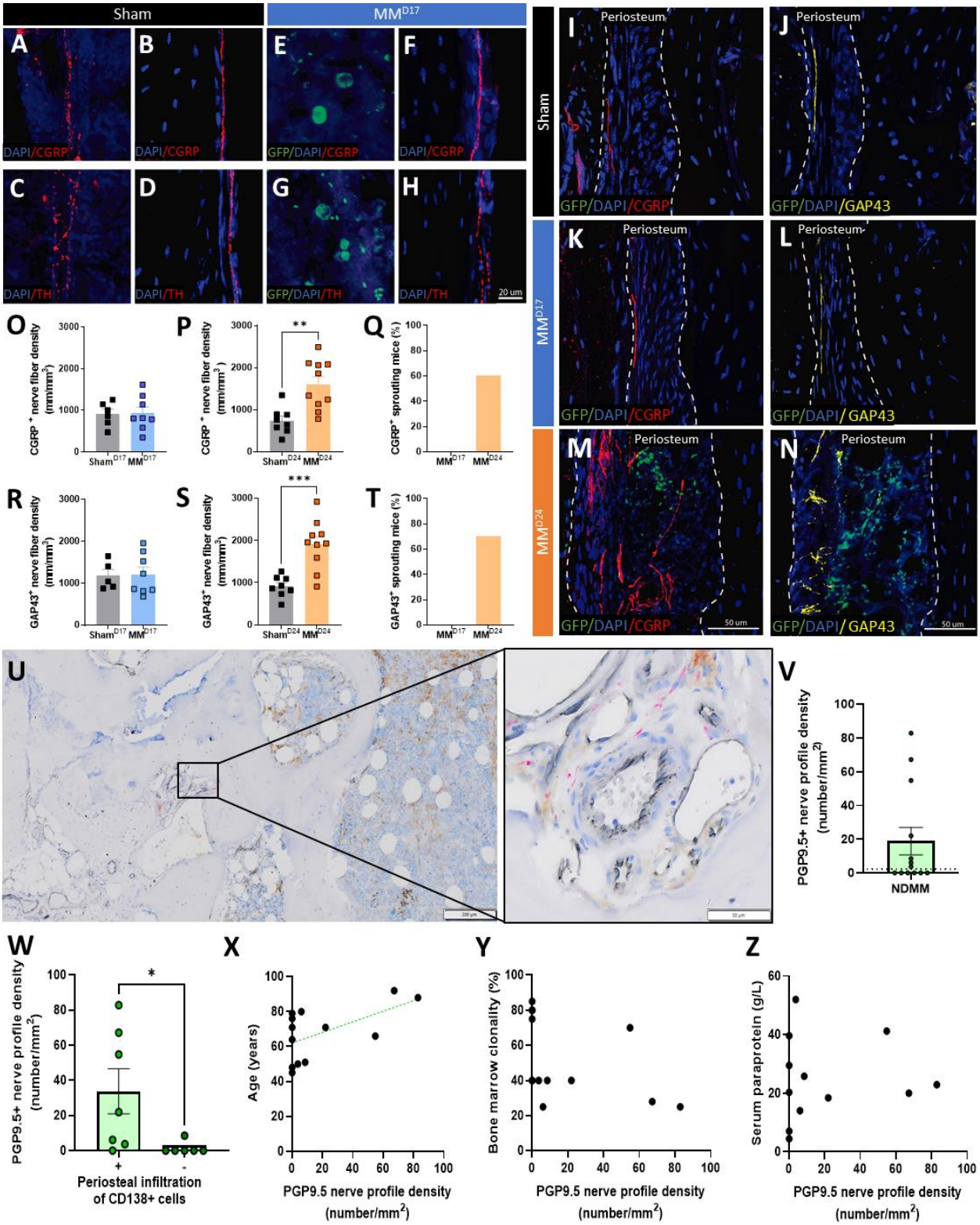

Figure 3. MM induces periosteal nerve sprouting in mouse and human tissue. (A-D) Representative images of CGRP^{+} (A, B) and TH^{+} (C, D) nerve fibres in the bone marrow (A, C) and periosteum (B, D) of sham mice. (E-H) CGRP^{+} (E) and TH^{+} (G) immunoreactivity is undetectable in the bone marrow of MM^{D17}, but visible in the periosteal compartment (F, H). (I-N) Representative images of CGRP^{+} (I, K, M) and GAP43^{+} (J, L, N) nerve fibres in the periosteum of sham^{D24} (I, J) and

MM^{D24} (M, N). (O, P) Quantification of relative $CGRP^+$ nerve fiber density on post-surgical day 17 (O), and 24 (P). **p<0.01 by unpaired, two-tailed Student´s *t*-test. (R, S) Quantification of relative $GAP43^+$ nerve density on post-surgical day 17 (R) and 24 (S). ***p<0.001 by unpaired, two-tailed Student´s *t*-test. (Q, T) Percentage of MM bearing mice presenting periosteal $CGRP^+$ (Q) or $GAP43^+$ (T) nerve sprouting at different time-points. (U) Cross sections of 3.5-µm trephine iliac crest bone biopsies from NDMM patients were triple stained for $CD138^+$, $CD34^+$ $PGP9.5^+$. (V) Quantification of $PGP9.5^+$ nerve fibres in the periosteum of NDMM patients; dotted line displays the previously reported human periosteal $PGP9.5^+$ nerve density (18). (W) Periosteal $PGP9.5^+$ nerve density in NDMM patients with or without $CD138^+$ cell infiltration to the periosteum. *p<0.05 by unpaired, two-tailed Student´s *t*-test. (X-Z) Correlation of $PGP9.5^+$ nerve density to age in NDMM. *p<0.05, r=0.57 by two-tailed Pearson correlation. (X, Z) Lack of correlation between periosteal nerve density and tumour burden measured as bone marrow clonality (Y) or serum paraprotein levels (Z). NDMM= Newly diagnosed multiple myeloma. Sham n= 6-8; MM n=8-9. NDMM n=13.

Pharmacological blockade of periosteal nerve sprouting induces a transient anti-nociceptive effect

Next, we tested the mechanistic role of periosteal nerve sprouting on MIBP using a therapeutic anti-netrin-1 blocking antibody (NP137). Netrin-1 is an axon guidance molecule known to play a pivotal role in neurogenesis through binding to its canonical receptors UNC5 homolog (UNC5H) and deleted in colorectal cancer (DCC) (19-21). Previous studies have demonstrated a role of netrin-1 on sensory nerve sprouting (22) and silencing Netrin-1 reduces resiniferatoxin-induced sprouting of myelinated afferent fibers and mechanical allodynia (23). To investigate whether blockade of periosteal nerve sprouting attenuated MIBP, sham and 5TGM1-GFP inoculated mice were systemically treated with vehicle (MM^{VEH}) or NP137 (10 mg/kg, i.p.; MM^{NP137}). Biweekly treatment with the anti-netrin-1 antibody delayed the onset of nociception, inducing a significant difference in limb use scores in MM^{NP137} at day 26 (Figure 4A, B); limb use scores were similar between MM^{NP137} and MM^{VEH} from post-surgical day 27. Moreover, NP137 treatment did not affect overall survival (Figure 4C) nor

tumour burden, as assessed by terminal splenomegaly (Figure 4D). To evaluate whether the transient analgesic effect was a consequence of decreased osteolysis, we performed µCT analyses of endpoint $sham^{VEH}$, MM^{VEH} and MM^{NP137} femurs. Our results demonstrated that netrin-1 blockage does not revert the BV/TV reduction induced by MM (Figure 4E). Moreover, the structural parameters of trabecular bone and bone mineral density were unchanged between MM^{VEH} and MMN^{P137} femurs (data not shown). To confirm the capacity of NP137 treatment to block periosteal nerve sprouting, we assessed the presence of $CGRP^{+}$ nerve fibres in the femoral periosteum of the treated mice. Our evaluation confirmed that NP137 treatment inhibits nerve sprouting, as MM^{NP137} mice showed $CGRP^{+}$ periosteal nerve density similar to sham, while MM^{VEH} ipsilateral femurs showed significant $CGRP^{+}$ nerve sprouting (Figure 4F, G); likewise, periosteal infiltration of MM cells was decreased in antibody-treated MM mice (Figure 4H). Anatomical presence of a microneuroma was observed in 25% of the vehicle-treated MM mice (Figure 4F), a feature of the disease never before described but that is consistent with animal models of solid bone cancers such as prostate (24) and breast (16) bone metastases or osteosarcoma (17, 25). The concentration of serum NP137 was significantly higher in serum of $sham^{NP137}$ mice compared to MM^{137} mice, potentially due to higher antibody clearance by the tumour (Supplementary Figure S2). Systemic antibody treatment by itself in sham mice had no effect on behaviour, bone structural parameters or neuronal innervation (data not shown).

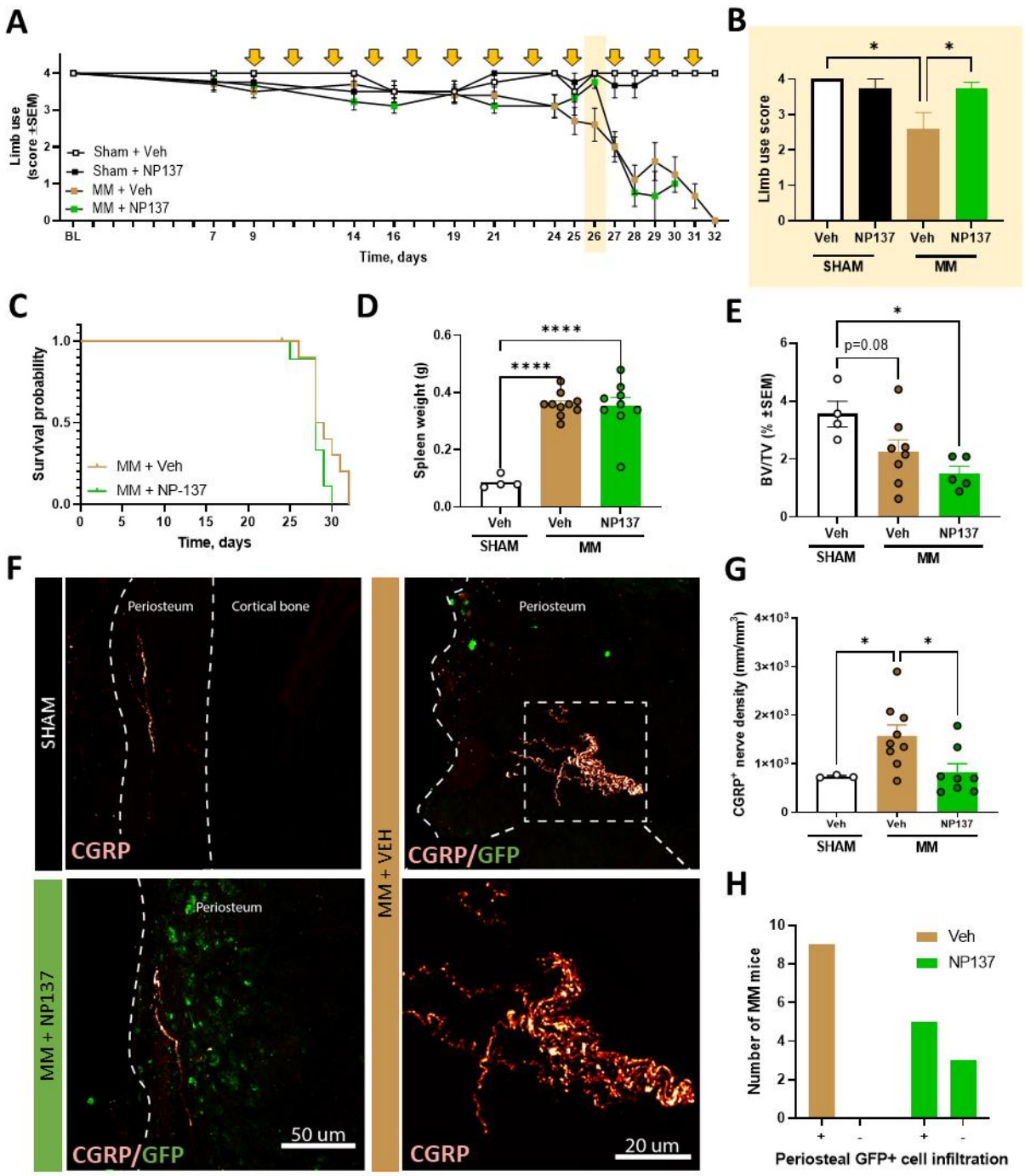

Figure 4. Pharmacological blockage of periosteal nerve sprouting induces a transient anti-nociceptive effect in 5TGM1-bearing mice. (A, B) Effect of anti-netrin-1 treatment (NP137 10 mg/kg, i.p.; dosing days represented by arrows) or vehicle on sham or MM mice. (B) Post-surgical day 26 limb use score of sham or MM mice treated with vehicle or NP137. *p<0.05 by one-way ANOVA followed by Holm-Šídak post-hoc test. (C) Survival plot of NP137 treated mice. (D) Endpoint spleen weight. ****p<0.0001 by one-way ANOVA followed by Holm-Šídak post-hoc test.

(E) Effect of systemic NP137 treatment on bone osteolysis, measured as bone volume per total volume (BV/TV). *p<0.05 by one-way ANOVA followed by Holm-Šídak post-hoc test. (F) Representative images of periosteal $CGRP^+$ nerve fibres and GFP^+ MM cells in sham and MM mice treated with vehicle or anti-netrin-1 treatment. (G) Quantification of $CGRP^+$ periosteal nerve density. *p<0.05 by one-way ANOVA followed by Holm-Šídak post-hoc test. (H) Number of vehicle- or NP137-treated MM mice presenting 5TGM1-GFP MM cell infiltration to the periosteum. MM= Multiple myeloma. Sham n=3-4; MM n= 5-10.

Dorsal root ganglia (DRG) transcriptomic dysregulation reveals MM infiltration

Following our observation of periosteal sprouting at the onset of nociception, we next hypothesized that MM invasion of the bone niche induces transcriptomic changes in the cell bodies of the innervating nerve fibres. However, considering that blocking of the nerve fibre sprouting only had a transient analgesic effect, there are clearly other mechanisms involved in MIBP. To test this, the DRG transcriptional signature of sham or 5TGM1-GFP inoculated mice during MIBP was evaluated. As expected, MM^{D24} animals displayed nociception (Figure 5A) and splenomegaly (Figure 5B), confirming disease development. On post-surgical day 24, RNA from lumbar DRGs L2, L3 and L4 was extracted and sequenced (if RIN>8), resulting in library sizes of 19-22M reads per sample. The mapping rates to the mouse transcriptome were similar across samples, ranging between 88-92% of all reads. We identified 1.389 differentially expressed genes (DEGs) between MM and sham groups with an FDR<5% (Figure 5C, D). Interestingly, the DRG transcriptomic signature of MM mice was highly heterogeneous across samples; this heterogeneity was not correlated to tumour burden (Figure 5D). However, significant changes in the expression pattern of DRG gene expression were driven by the presence and transcriptional level of green fluorescent protein (GFP) (Figure 5D), suggestive of MM infiltration to the DRG. Next, we performed gene set enrichment analyses (GSEA) to better interpret the transcriptional dysregulation by taking into account the entire set of genes expressed in our data and without setting up any arbitrary threshold of statistical significance on differential

expression. GSEA for GO BP (Gene Ontology biological process) terms and Reactome pathways indicated that the main dysregulated signaling pathways in MM mice were related to cell cycle, immune response (activated) and neuronal signaling (suppressed) (Supplementary Figures S3 and S4).

Next, we compared the MIBP transcriptomic signature with that of six other models encompassing different painful conditions, as compiled by Bangash et al. (26). These included (Figure 5E) mouse models of painful lung cancer metastasis to the bone (cancer), partial sciatic nerve ligation (PSL), mechanical joint loading (MJL), chemotherapy induced peripheral neuropathy (Oxaliplatin), chronic muscle pain (CMP) and inflammation (Complete Freund´s Adjuvant, CFA). To identify similarities among different painful conditions, we first examined the overlap between the set of MIBP DEGs, and the top 300 genes with smallest p-values from each of the six conditions. Our analyses indicate that MIBP has most DEGs congruent with the PSL and CFA models, suggesting a neuropathic and an inflammatory component (Figure 5E).

Next, we performed (GSEA) for the 6 models and compared results by selecting the top 40 enriched GO BP terms or Reactome pathways in MIBP and visualizing their normalized enrichment score and corresponding adjusted p-values across all models (Figure 5F and Supplementary Figure 4). Interestingly, the transcriptional signature of MM was overall most similar to that of PSL, suggesting a strong neuropathic component in MIBP. These results are in line with our previous finding of periosteal nerve sprouting as a contributing mechanism to MIBP. Even though the overlap of DEGs is higher with the CFA model, the comparative GSEA analysis indicates that this similarity is only retained at the level of common activated inflammation-related pathways. Since spinal microglial reaction is a well-known feature of neuropathic pain (27, 28), we characterized the expression of ionized calcium-binding adaptor molecule 1 (Iba1) and phospho-p38 mitogen-activated protein kinase (Pp38 MAPK) in the dorsal horn of the spinal cord of $sham^{D24}$ and MM^{D24} mice. No changes in relative $Iba1^{+}$ or $Pp38^{+}$ cell number were observed at any lumbar region (Supplementary Figure

S5). Likewise, no changes in glial fibrillary acidic protein (GFAP) staining were observed, suggesting that astrocytosis is not a main feature of MIBP (Supplementary Figure S5).

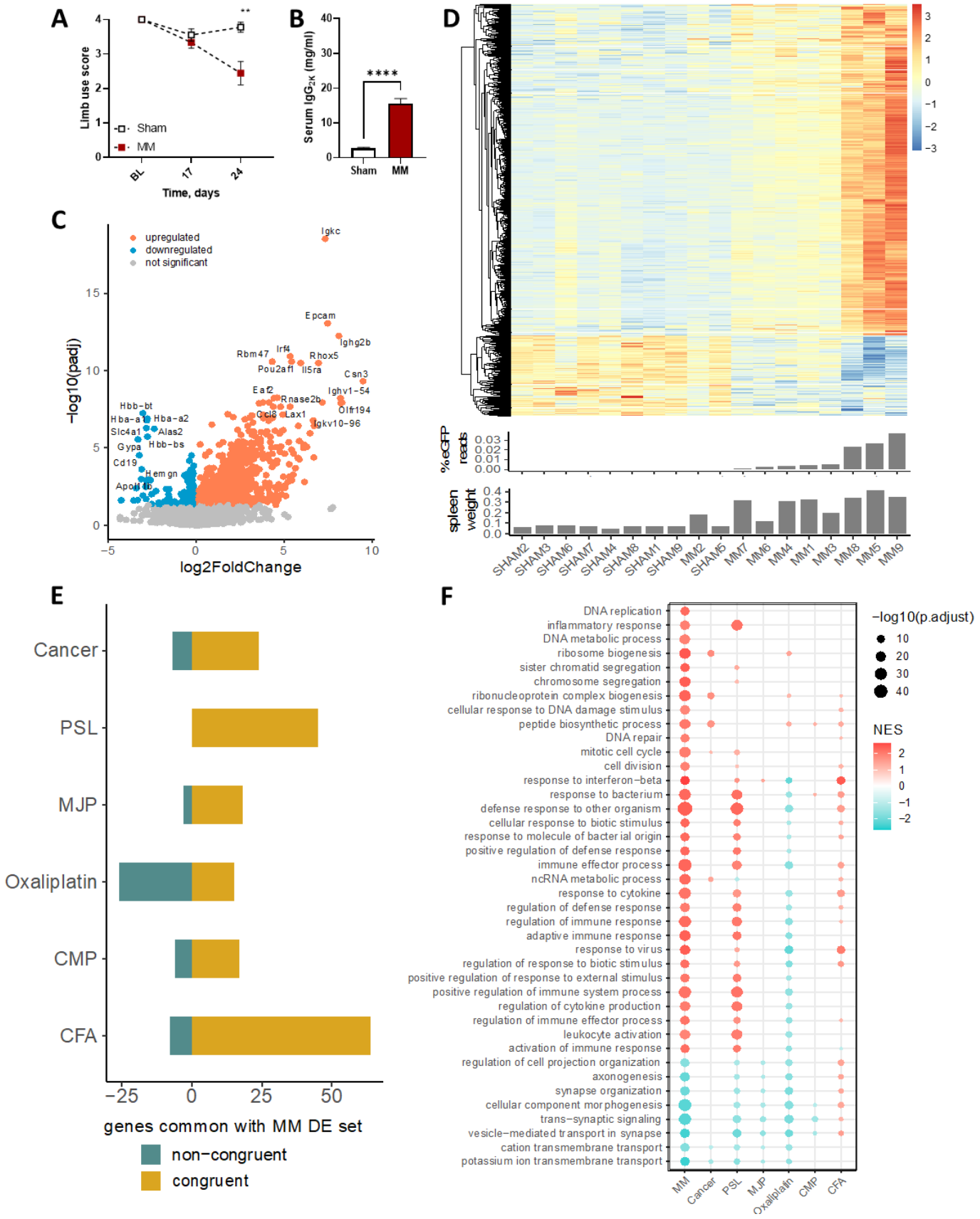

Figure 5. The DRG transcriptional signature in MM unveils MM infiltration to the nervous system and a strong neuropathic component. (A, B) Development of nociception (A) and splenomegaly (B) were confirmed prior to DRG isolation and transcriptomic analyses. ** $p<0.01$ by Friedman´s two-way test followed by Wilcoxon´s two-sample test and ****$p<0.0001$ by unpaired, two-tailed Student´s t-test. (C) Volcano plot showing the log2 fold change of differentially expressed genes (DEGs) between sham^{D24} and MM^{D24}. (D) Heatmap depicting z-scaled regularized log counts of the 1389 DEGs identified between sham and MM lumbar DRGs (adjusted p-value<0.05). The heterogeneous transcriptome of MM DRG was correlated to the presence and levels of GFP expression. (E) Comparison to other mouse pain models in terms of common DEGs. The overlap between the DEGs identified in MM mice and top 300 DEGs, sorted by p-value, in other painful models, as reported by Bangash et al (26), highlights the neuropathic and inflammatory component of MIBP. In yellow, common DEGs congruent in their direction of regulation between MM and each of the other models; in blue, common DEGs in non-congruent direction of regulation. (F) Model comparison in terms of GSEA. Normalized enrichment scores (NES) and their corresponding p-values for the top 40 enriched GO terms in MIBP are displayed across all seven pain models(26), indicating that the PSL model is the most similar to MIBP. MM= Multiple myeloma. PSL= Partial sciatic nerve ligation. MJP= Mechanical joint loading. CMP= chronic muscle pain. CFA= Complete Freund´s adjuvant. Sham n=9; MM n=9.

MM infiltration and increased ATF3 expression in DRGs from MM^{D24} mice.

To further verify that the GFP reads detected during transcriptome sequencing were caused by MM infiltration to the DRG and not the result of sample contamination, we performed immunofluorescent GFP staining on the ipsilateral DRGs of sham and MM bearing mice euthanized on post-surgical day 17 or 24 (Figure 6A). We found 5TGM1-GFP infiltration in the ipsilateral L2 DRG of all MM^{D24} mice confirming the results from the transcriptomic analysis. Similar results were found in the ipsilateral L3 (data not shown). No GFP expression was detected in DRGs of MM^{D17} and sham

controls (Figure 6B, C). Thus, our data indicate that MM has the capacity to metastasize to the peripheral nervous system, which occurs concomitantly to development of nociception.

Next, we examined the integrity of DRG vascularization and potential neuronal damage through immunofluorescent staining of the ipsilateral DRG of sham and MM mice 17 or 24 days after cell inoculation. Our analyses of $CD31^{+}$ blood vessels (Figure 6D) revealed a significant decrease in blood vessel length (Figure 6E, H, K) and density (Figure 6F, I, L) in DRGs from MM^{D24}, but not MM^{D17}, compared with sham at all the analysed lumbar levels. The proportion of sympathetic TH^{+} neurons was similar across samples (Figure 6G, N); however, the percentage of activating transcription factor 3 $(ATF3)^{+}$ neuron profiles was significantly increased in ipsilateral MM^{D24} as compared to $sham^{D24}$, suggesting tumour-induced neuronal injury (Figure 6J, M). Additionally, ATF3 and 4′,6-diamidino-2-phenylindole (DAPI) staining revealed a specific pattern of nuclear staining consistent with the development of Nagoette nodules, indicative of neuronal degeneration (29) (Figure 6O). Finally, we examined the contralateral MM^{D24} DRGs and found intact vasculature, low levels of ATF3 expression and extragangliar presence of GFP^{+} MM cells (Figure 6P), suggesting that MM DRG infiltration and consequent vasculature and neuronal damage may be specific mechanisms of MIBP.

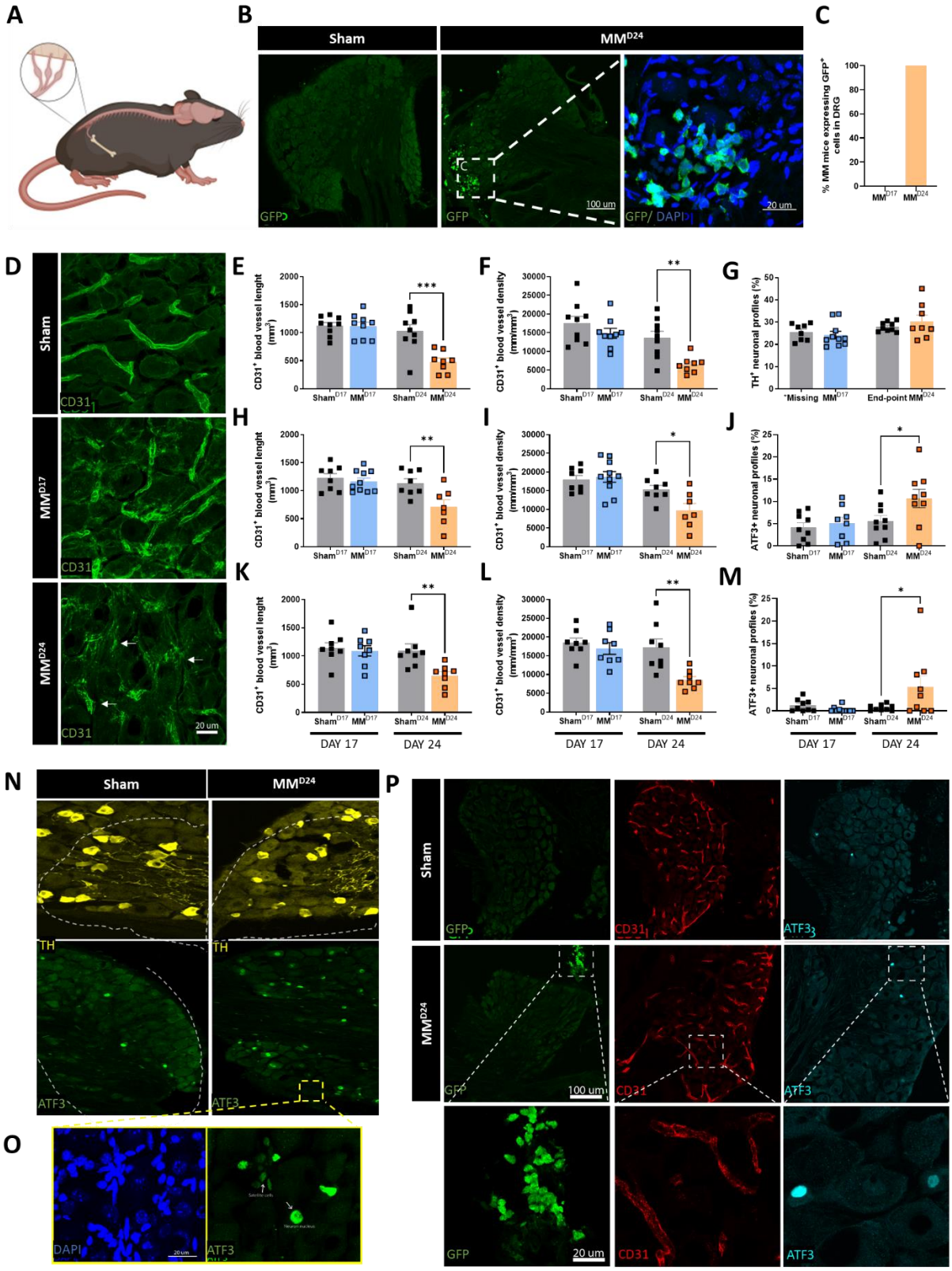

Figure 6. MM cells metastasize to the DRG causing damage to vasculature and neuronal bodies. (A) Ipsilateral and contralateral lumbar DRGs L2, L3 and L4 were collected. (B) Frozen sections from L3 DRGs were immunostained for GFP. (C) Number of MM bearing mice presenting GFP$^+$ staining in the ipsilateral L3 DRG. (D) Representative images of CD31$^+$ immunostaining in DRG

frozen sections. Note the structural injury to $CD31^+$ blood vessels in MM^{D24}, indicated by white arrows. (E, H, K) Quantification of $CD31^+$ blood vessel length in the ipsilateral L2 (E), L3 (H) and L4 (K) DRGs. **p<0.01, *** p<0.001 by one-way ANOVA followed by Holm-Šídak post-hoc test. (F, I, L) Quantification of relative $CD31^+$ blood vessel density in the ipsilateral L2 (F), L3 (I) and L4 (L) DRGs. *p<0.05, **p<0.01, *** p<0.001 by one-way ANOVA followed by Holm-Šídak post-hoc test. (G, N) TH^+ immunostaining (G, top panel) and quantification (N) in frozen sections from L2 DRGs. (J, M, N) $ATF3^+$ immunoreactivity (N, bottom panels) and quantification in L2 (J) and L3 (M) DRGs. **p<0.01, *** p<0.001 by one-way ANOVA followed by Holm-Šídak post-hoc test. (O) High-resolution imaging of $ATF3^+$ and DAPI immunoreactivity on ipsilateral L2 MM^{D24} DRG. Note the presence of Nagoette nodules denoted with white arrows, suggestive of neuronal degeneration. (P) Frozen sections from contralateral MM^{D24} DRGs were stained for GFP, CD31 and ATF3. Extragangliar 5TGM1-GFP^+ MM cells were observed in the contralateral DRGs. MM= Multiple myeloma. Sham n=8-9; MM n= 7-10.

The transcriptomic DRG signature of a MM patient suggests metastatic infiltration

Following our unexpected observation of MM metastasis to the DRG of myeloma-bearing mice displaying MIBP, we questioned the translational validity of our findings. To evaluate whether the genetic signature of MM cells was present in peripheral nervous system of a MM patient, we accessed the transcriptome of 68 DRGs collected from 39 patients with 18 different types of cancer (30), as well as that of two thoracic DRGs from one MM patient. First, we used publicly available datasets to generate a transcriptomic signature of composed of human markers generally expressed in MM cells (31-33) that show low or no expression in healthy DRG tissue (34). Datasets were chosen to represent different high throughput technologies (Affymetrix, bulk RNA-seq and single cell RNA-seq) and the final MM signature contained 40 genes that were ranked within the top 10,000 genes in Affymetrix and bulk-RNA, detected in over a third of single-cell RNA-seq cells, and had an expression rank

<0.75 TPM in normal DRG tissue. Gene expression of the 40 signature markers was generally higher in the DRGs of the MM patient compared with most other cancer samples (Figure 7A). Indeed, the distribution of percentile gene expression of the two MM samples over the other cancer samples, across the 40 MM markers, showed a general shift towards higher percentiles (Figure 7B), with a mean percentile of 71,6 (mean of the two samples from the MM patient). In order to check whether other cancer samples displayed a similarly high or higher MM signature, we plotted the mean percentile marker distribution for all other 68 cancer samples and confirmed that MM samples showed among the highest mean percentile (Figure 7C). Other samples with a high mean percentile (indicative of similarly enriched expression for the selected marker genes) were DRGs from prostate and renal cell carcinoma patients (Supplementary File S2).

Next, we asked if the MIBP transcriptomic signature identified in our animal experiments was translatable to the human condition. Since the DEGs observed in MM^{D24} vs $sham^{D24}$ mice seemed to be largely driven by MM cell infiltration to the DRG, we hypothesized that these DEGs are either expressed in MM cells or disrupted as a result of MM infiltration and could be used as a proxy for MM metastasis in patient data. Thus, we selected the set of human orthologs to the mouse upregulated DEGs (padj<0.05) in MM^{D24}, resulting in a set of 797 genes. Like with the human datasets, the relative gene expression of the chosen markers displayed a distribution shift towards higher percentiles, indicating a tendency towards overexpression of the genes from this set in the human MM DRGs compared to other cancers (Figure 7D). The MM samples showed among the highest mean percentile (mean of the two MM samples - 66,4) (Figure 7E). Taken altogether, our data suggest that cancer metastasis to the DRG may also occur in MM patients.

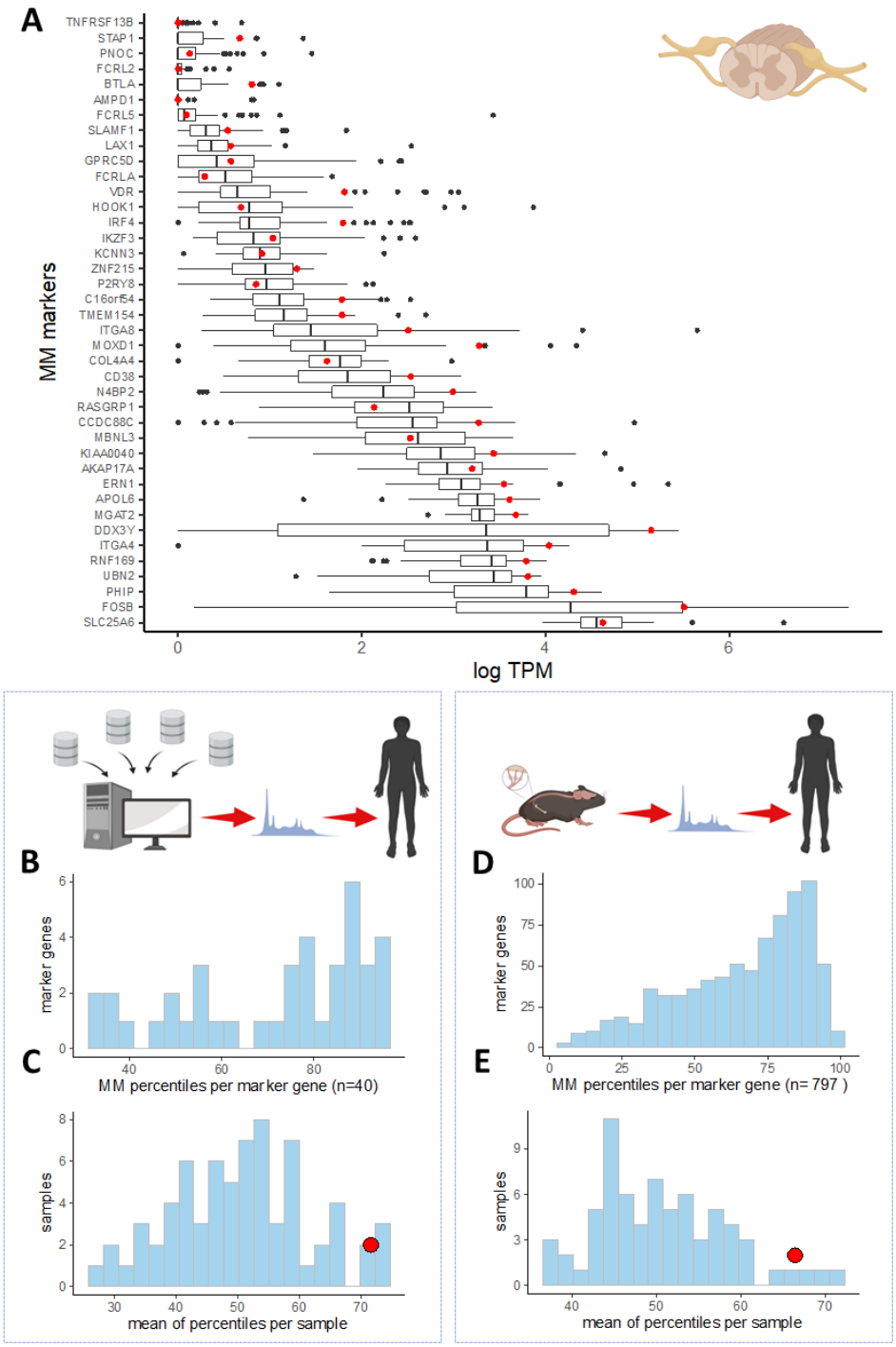

Figure 7. The transcriptomic signature of a MM patient suggest cancer infiltration to the DRG. (A) Box-plot of log FPKM counts for the 40 signature MM markers across 70 DRGs from cancer patients. Red dots indicate the mean expression level in two thoracic DRGs from one MM patient. (B) Distribution of percentile gene expression for all 40 markers in the DRGs of the MM patient. (C) Distribution of mean percentiles across all cancer samples; red dot indicates the mean percentile for the MM patient. (D) Distribution of percentile gene expression for the signature set derived from the mouse MM^{D24} upregulated DEGs (padj<0.05). (E) Distribution of mean percentiles across all cancer

samples; red dot indicating the mean percentile for the MM patient, for the mouse MM^{D24} derived set.

Discussion

Bone pain remains among the main complaints from MM patients and significantly impairs their quality of life; indeed, previous reports have highlighted that MM patients report more symptoms and problems than leukaemia and lymphoma patients (35). However, the preclinical search for adequate analgesic options for MIBP is scarce and pathophysiological mechanisms underlying bone cancer pain are poorly understood (9, 36, 37).

In this study, we use our previously characterized local immunocompetent mouse model of MIBP (9) to investigate disease-driven alterations of the central and peripheral nervous system that may lead to rational search of new analgesic targets. Following 5TGM1-GFP cell transplantation into the intrafemoral marrow of a tumour-permissive mouse strain, we observed the progressive development of non-stimulus evoked nociceptive behaviours that can be considered as surrogate markers of spontaneous pain and/or wellbeing (38, 39). We have previously characterized this localized model and shown that systemic opioid administration (10 mg/kg morphine) on post-surgical day 26 reverses the MM induced deficits in limb use, further confirming model validity (10).

Following the direct transplantation of 5TGM1-GFP cells into a permissive microenvironment, we observed trabecular bone loss as early as post-surgical day 17, prior to the development of nociception. This apparent disconnection between osteolytic damage and nociception is consistent with preclinical and clinical evidence highlighting the limited analgesic efficacy of commonly used anti-resorptive treatments such as bisphosphonates (6, 10, 11, 40). In contrast, we observed cortical osteolysis at later stages of the disease, coinciding with the onset of nociception and suggesting periosteal involvement in MIBP. To confirm this, further immunostaining demonstrated 5TGM1-GFP cell escape to the periosteum of these bones, along with significant sprouting of sensory neurons, concomitant to nociception. Periosteal nerve sprouting has been posed as a potential mechanism of

cancer-induced bone pain in animal models of breast (16) and prostate bone metastasis (24), as well as osteosarcoma (17), and anti-NGF therapy has recently showed modest results for the treatment of cancer pain (41). Our results support the hypothesis that myeloma cells cause osteolytic cortical lesions through which they escape to the periosteum, where they may release neurotrophic factors that promote nerve sprouting and, potentially, nociception. The translational implication of these pre-clinical results was further supported by our observation of increased periosteal nerve density in NDMM patients compared patients with hyperparathyroidism (18), and the observation that periosteal sprouting occurred more frequently in patients with periosteal infiltration of MM cells.

To evaluate the contribution of periosteal nerve sprouting to MIBP, we tested the effect of repeated systemic NP137 administration. NP137 is a humanized monoclonal antibody targeting Netrin-1 that is currently undergoing Phase I and II clinical trials (NCT02977195; NCT04652076) as an anti-cancer treatment. Because Netrin-1 is a neurotrophic ligand involved in axon guidance, we expected that NP137 treatment would prevent periosteal nerve sprouting and, consequently, MIBP. Our results demonstrated that netrin-1 blockage effectively prevents periosteal nerve sprouting in myeloma-bearing mice without affecting bone morphometry. In contrast to previous studies (42), systemic NP137 administration failed to have an effect of tumour burden or survival. While the reasons for this discrepancy are unknown, serum levels of sham drug-treated mice were twice as high compared to those of MM drug-treated mice, suggesting increased antibody clearance and volume distribution in MM-bearing mice. Future studies with greater doses of this antibody in mice with MM are warranted to determine its effect on tumour disease progression.

Next, we evaluated the transcriptional DRG signature of MIBP and compared it to that of other pain models, including bone cancer metastasis, peripheral neuropathy, inflammation and chemotherapy-induced bone pain as previously described (26). Our data suggested that the transcriptional signature of MM bone pain was more similar to that of neuropathic and inflammatory pain than the other pain models. Detailed examination of the spinal cord in MM and sham mice revealed neither microglia activation not astrocyte reaction in the dorsal horn of the spinal cord at any investigated time-point.

While it has been speculated that central-acting agents targeting sensitization (i.e. gabapentin and antidepressants) may pose an alternative for the management of MIBP (6), there is a lack of evidence supporting this treatment line. Our results stride away from these treatment options, as we did not find signs of disease-induced central sensitization at any spinal lumbar level. However, we and others have previously reported that spinal microglial reaction in cancer-induced bone pain models is a highly variable occurrence that may not reflect the clinical reality (43, 44). Instead, the neuropathic component of MIBP is in line with clinical reports describing baseline peripheral neuropathy in a proportion of MM patients (45, 46), which is also used as a prognostic factor of chemotherapy induced peripheral neuropathy and treatment outcome in this patient population (47). These results, in combination with our observation of periosteal nerve sprouting, suggest that medications targeted to neuropathic pain patients may be useful to treat a fraction of myeloma bone pain patients. However, our approach has several limitations, including that the GSEA comparison between our MM model and those described by Bangash et al (26) is directly impacted by the quality of the data from each of the models. Thus, while the PSL model was the most similar to MM, it was also the one showing the highest statistical significance for the DEG analysis and resulted also in a higher number of significant GSEA terms; in contrast, cancer, CMP and MJP models (i.e. those with the lowest degree of similarity to MM) showed no DEGs falling within the threshold after FDR correction for the models, which may hinder the significance of our findings.

Among the most important findings from our mouse transcriptomics analyses was the high heterogeneity in the pattern of DEG in MM mice. Interestingly, the MIBP transcriptional signature was not correlated to surrogate markers of tumour burden or nociception but was instead highly dependent on the number of GFP counts. These results strongly suggest MM metastases to the ganglia, a never-before described feature of the disease that we further confirmed through immunohistological staining. Along with the spatial localization of MM cells in the ganglia, we observed structural damage and decreases in length and density of blood vessels innervating the lumbar ganglia. Whether damage to the blood vessels occurs prior to neoplastic infiltration (thus

allowing the passage of MM cells into the DRG) or is a consequence of it, remains to be elucidated. Our observation of GFP^+ MM cells in the surrounding of contralateral ganglia supports the later, but further studies are needed to clarify the sequence of events. In any case, neoplastic infiltration of the ganglia caused neuronal damage, demonstrated by the increase in $ATF3^+$ nerve profiles and the formation of nodules of Nagoette (29). This novel observation of myeloma-induced neuronal degeneration presents a new research avenue that requires further research to identify potential treatment targets.

Our human transcriptomic analyses revealed a similar indication of possible neoplastic infiltration in the DRGs of a MM patient. To our knowledge, the only previous publication addressing this question is from 1958, when Dickenman et al. (48) found degenerative changes but no cancer infiltration in the DRGs of eight deceased MM patients. In contrast, we have performed bulk sequencing of two thoracic DRGs from a MM patient and compared our transcriptomic results to those of 39 patients with other cancer types. Comparing our custom-made MM transcriptional signature composed by MM genes with low or no expression in healthy DRG as per publicly available datasets to the gene expression profile of all 70 DRGs suggested that MM gene expression was enriched in the DRGs from the MM patient. Similarly, evaluating the expression pattern of human orthologs to DEG identified in MIBP mice revealed enrichment in the MM patient DRGs. This observational data supports the translational validity of our findings with the obvious limitation of the highly restricted sample number. Accessing quality human DRG tissue is challenging, but further research is needed to conclude whether cancer metastasis to the DRG is indeed a common occurrence in MM patients.

In conclusion, our data suggests that MIBP is mediated by concomitant mechanisms including periosteal nerve sprouting and neoplastic infiltration of the DRG. Moreover, the transcriptional signature of MIBP indicates a neuropathic component and pain management in MM patients may require a multi-targeted approach that include drugs targeting neuropathic pain.

Funding and competing interests

This study has been funded by IMK Almene Fond and Brødrene Hartmanns Fond. Part of the work was funded by the Novo Nordisk Foundation (NNF14CC0001). The funding bodies played no role in data collection, analyses, or interpretation, nor in manuscript preparation. The authors disclose no competing interests.

Acknowledgements

The authors thank Kaja Laursen, Camilla S. Dall and the animal technicians from the Department of Drug Design and Pharmacology at University of Copenhagen. We also thank the patients for providing their time and agreeing to be part of this project. Figures have been made in Biorender.

Authors´ contributions

MDC and AMH: study conceptualization, funding acquisition and manuscript preparation. MDC, LJ, MAL, TLA, JMJA and AMH: study design. MDC, TN, DMT, NACS, JAVM, LPG, HE, DN, PMD MAL, JMJA and AMH: mouse experiments and data processing. MDC, OP, LJ and AMH: planning, performing and analysing the transcriptomics mouse experiment. MDC, JC, TJP, PMD, OA: planning, performing and analysing human transcriptomics data. MDC, REA, AM, ADC, TLA and AMH: collection and analyses of human bone biopsies.

Materials and methods

Cell culture

Mouse 5TGM1-GFP cells passaged *in vivo* were grown in suspension in RPMI media containing glutamine and phenol red, 1% penicillin/streptomycin (100U/100µg/ml), 1% sodium pyruvate (1mM), 1% MEM non-essential amino acids and 10% FBS, at 37°C and 5% CO_2. All reagents were purchased from Thermo Fischer Scientific, Denmark.

Animals

Male 5 to 7-weeks-old C57BL/KaLwRijHsd mice from Envigo (Venray, Netherlands) were housed in a temperature-controlled (22 ± 2 °C) room with 50% relative humidity under a 12:12 light:dark cycle (lights on a 07:00 AM). Mice were housed in groups of 4 or 5 in standard individually ventilated GM500^{+} cages (524 cm^{2}) in a mouse-dedicated room and allowed to acclimatize >7 days prior to experimental allocation. Cages were enriched with red translucent shelter, an S-brick, paper ropes and corn hidden in the bedding (Tapvei 2HV bedding, Brogaarden, Gentofte, Denmark). Food (Altromin 1314; Brogaarden, Gentofte, Denmark) and water were provided *ad libitum*. Experiments were conducted in accordance with the Danish Act on Animal Experiments (LBK No. 474 of 15/05/2014) and approved by the Danish animal Experiments Inspectorate. This manuscript is reported in accordance to the ARRIVE 2.0 guidelines.

Experimental design

In a time-course study, mice were intrafemorally inoculated with 5TGM1-GFP myeloma cells or vehicle, their behaviour analysed over time, and euthanized at two different time-points (i.e. post-surgical day 17 and 24, respectively) by transcardial perfusion before tissue collection. In the transcriptomics experiment, DRGs from 5TGM1-GFP or vehicle-bearing mice were collected and fresh frozen for further RNA extraction and transcriptome sequencing 24 days after surgery. In the NP137 experiment, mice were dosed with NP137 (10 mg/kg, i.p.) or vehicle biweekly, their behaviour analysed over time and euthanized at end-point by transcardial perfusion before tissue collection. All behavioural testing was carried out in a quiet room during the light phase (between 07:00 AM and 19:00 PM) by the same researcher, who was blinded to experimental group. Mice were randomized according to baseline burrowing capacity or weight. Good laboratory practices are described in the Supplementary Table S1 (see Supplementary File S1); all materials are available upon request.

Model induction

Mice were anaesthetized with ketamine/xylazine cocktail (85,5 mg/kg Ketaminol vet- MSD Animal Health, The Netherlands- and 12,5 mg/kg Nerfasin vet – Virbac, Kolding, Denmark; i.p.); eye ointment was applied to prevent dryness (Ophta A/S, Actavis Group, Gentofte, Denmark). Upon

confirmation of loss of pedal reflex, the mouse was placed on a heating pad and an incision (<1 cm) was made above the right anterior knee upon its shaving and disinfection with 70% ethanol. The retinaculum tendon was slightly displaced, and the patella ligament pushed to the side, exposing the distal femoral epiphysis, where hole was drilled with a 30G needle. Through an insulin needle (0.3 mL; BD Rowa Technologies, Lyngby, Denmark), 10-µl of vehicle (Hank Balance Salt Solution, Gibco, Denmark) or cell suspension ($5x10^4$ 5TGM1-GFP cells) were inoculated into the intramedullary femoral cavity. The hole was closed with bone wax (Mediq Danmark A/S, Brøndy, Denmark), the patella pushed back into place, and the incision closed with surgical clips (Agnthos, Lidingö, Sweden). Mice received 0.5 mL saline (s.c.) and two bolus injections of carprofen (5mg/kg, s.c.; Pfizer, Ballerup, Denmark), one before surgery and another 24 h after.

Limb use

The limb use of freely walking animals was scored as: 4= normal gait; 3= insignificant limping; 2= significant limping and shift in bodyweight distribution towards the healthy limb; 1= significant limping and motor impairment; 0= paraplegia, as previously described (10). Briefly, mice were acclimatized with their cagemates to a standard transparent cage of 125 x 266 x 185 mm for ≥10 min. Then, mice were individually transferred to a similar cage where their gate was observed for 3 min.

Burrowing

Burrowing capacity was assessed as amount of sand (0-3 mm diameter, ScanSand, Herlev, Denmark) displaced from a burrowing apparatus during a 2-hour burrowing session (38). The burrowing apparatus consisted of a grey opaque plastic tube (200 mm x 72 mm diameter; frontal end raised 30 mm from the ground) filled with 500 g of sand and placed in a transparent plastic cage (125 x 266 x 185 mm) without bedding, closed with a grid lid. Prior to baseline measurements, mice were placed in pairs in the cage containing an empty burrowing apparatus for 2 h. On the second and third day, this procedure was repeated but the burrowing tube was filled with 500 g of sand. Throughout the experiment, burrowing was conducted at the same time and in the same room in absence of the researcher.

Tissue extraction and analyses

Mice were deeply anaesthetized with a ketamine/xylazine cocktail, as described. Upon loss of pedal reflex, mice were pinned down on their dorsal side and their abdomen and thoracic cage were opened, exposing the beating heart. Transcardial blood was collected with a 27G needle, before transcardially perfusing with 21-28 ml of ice-cold PBS and 4%PFA-0,12% picric acid (Merck, Søborg, Denmark). Spleens were excised and weighed. Ipsilateral femurs were collected, post-fixated 24 h in 4% PFA and stored in 70% ethanol until µCT analyses were performed, and in 0.1M PBS afterwards. Spinal cords and lumbar DRGs were post-fixated 24 h in 4%PFA-0,12% picric acid, dehydrated in 30% sucrose and embedded in OCT (Sakura, Japan). In the transcriptomics experiment, mice were perfused with 10-ml of ice-cold PBS and their lumbar DRGs quickly extracted and fresh-frozen in RNAse-free Eppendorf tubes in a 3-Methylbutanol freezing bath.

Serum IgG_{2b} analyses

Blood was left undisturbed at RT for 30-90 min and thereafter centrifuged 10 min at 4 °C and 6000 RPM. Serum was stored at -80°C and IgG_{2b} was measured with a sandwich ELISA kit (Bethyl Laboratories, #E99-109; AB_2892024) following manufacturer´s recommendations.

µCT analyses

Ipsilateral femurs were analysed in a SkyScan 1272 ex vivo scanner at 50 kilovots (kV) and 200 mA, as previously described (49). A 0,5 mm aluminium filter and a pixel size of 4,3 mm^2 were used. Following standard guidelines (50), the following morphometric parameters were assessed: bone volume per total volume (BV/TV), bone surface per bone volume (BS/BV), bone surface per total volume (BS/TV), trabecular thickness (Tb.Th), trabecular spacing (Tb.Sp), trabecular number (Tb.N) and lesion area. Representative 3D models were recreated with ParaViewSoftware (Clifton Park, NY, USA). For the anti-netrin experiments, scans were reconstructed using NRecon software (version 1.6.1.1; SkyScan) within a dynamic range of 0 to 0.15 and a ring artifact reduction factor of 5%. Reconstructed images were analyzed using CTAn (version 1.9.1.1 Bruker, Belgium). Analysis was done on the cross-sectional images of the tibias or femurs at 1.2 mm (offset) from the distal break in

the growth plate (reference point), on a fixed 1-mm region. The trabecular bone was carefully traced on all cross-sectional images of the distal femur and BV/TV was calculated.

Immunohistochemistry in lumbar DRGs

Lumbar DRGs were serially sectioned at 16-µm thickness. Slides were washed thrice, permeabilized in 0.1% Triton X-100/T-PBS and blocked with 1% BSA or 3% NDS before antibody labelling against activating transcription factor 3 (ATF3; either 1:200 polyclonal, rabbit anti-mouse, Novusbio, Abingdon, United Kingdom; #NBP1-85816, AB_11014863, or 1:400 polyclonal, rabbit anti-mouse, Santa Cruz, Dallas, Texas; #SC-188, AB_2258513), tyrosine hydroxylase (TH), a marker for post-ganglionic sympathetic neurons (TH polyclonal rabbit anti-mouse; 1:1000, Millipore; #AB152, AB_390204), CD31, a marker of blood vessel endothelial cells (CD31 monoclonal rat anti-mouse, 1:500, BD Pharmingen , San Diego, CA; #557355, AB_396660), or GFP (GFP polyclonal chicken anti-mouse; 1:2000, Invitrogen; #A10262, AB_2534023). After, slides were washed and incubated 3 h with secondary antibodies: Alexa Fluor 488 (Anti-rabbit, 1:1000, Invitrogen, Themo Fisher Scientific, Slangerup Denmark, #A11008, AB_143165), Cy3 (monoclonal donkey anti-rabbit 1:600; Jackson ImmunoResearch; #711-165-152, AB_2307443), Cy2 (polyclonal donkey anti-chicken, 1:400; #703-225-155, AB_2340370). Sections were counterstained with DAPI (1:10,000, Sigma Aldrich; #D21490) for 5 min, dehydrated in an alcohol gradient and rinsed in xylene. Slides were mounted DPX or fluorescent mounting medium containing DAPI (DAKO Agilent, Glostrup, Denmark).

DRG neuronal profile quantifications

Serial DRG sections were separated by >120 µm to prevent duplicate counting of neuronal cell bodies. At least a confocal image from three different sections under a 20X objective per animal was taken on a Zeiss LSM 800 confocal microscope (Jena, Germany). The number of $ATF3^+$ or TH^+ immunoreactive neuronal profiles in sensory ganglia were determined in Image J (NIH), as previously reported (51), by quantifying both labelled and non-labelled neuronal profiles.

DRG blood vessel quantifications

Quantification was performed by counting the number of $CD31^+$ blood vessels per unit volume (area x thickness) (52-54), where blood vessels were identified as $CD31^+$ and 2–10 μm in diameter; $CD31^+$ branched blood vessels were counted as one single vessel (55).. DRG sections were initially scanned at low magnification (10×) to identify the areas with the highest density of $CD31^+$ blood vessels and then a confocal image was obtained at 40× magnification. At least three pictures per animal were taken. An extended depth of focus processing was performed on all Z-stack files for each image and total number and length of $CD31^+$ blood vessels within cell body-rich areas (56) were determined using Image J (NIH). Then this area was multiplied by the thickness of the section (16 μm).

Immunohistochemistry in femurs

Following μCT, femurs were decalcified in 10% EDTA for two weeks at 4°C prior to cryoprotection in 30% sucrose and 4°C storage; decalcification was monitored using a portable x-ray equipment (Fona X70, Fona, Assago, Italy). Femurs were longitudinally cut in a frontal plane (25-μm thickness) with a cryostat (Leica 1900, Leica Biosystems, Il, USA), mounted on slides (Superfrostplus, Thermo Scientific; #J1800AMNZ) and allowed to dry (30 min, RT). Subsequently, slides were placed in vertical chambers (Shandon, Sequenza Immunostaining, Fisher Scientific; #73-310-017), washed, blocked (3% normal donkey serum, 0.3% triton X-100 in PBS) for 2 h RT and incubated o/n with a primary antibody cocktail containing anti-GFP antibody (polyclonal chicken anti-GFP, 1:2000; #A10262, AB_2534023; Thermo Fisher Scientific, Rockford, IL, USA) , anti-TH antibody (TH polyclonal rabbit anti-mouse; 1:1000, Millipore; #AB152, AB_390204), and an antibody against calcitonin gene-related peptide (CGRP; polyclonal rabbit anti-rat, 1:5000; #C8198, AB_259091; Sigma-Aldrich, St. Louis, MO, USA) or growth associated protein-43 (GAP43; rabbit anti-GAP43; 1:1000; #AB5220, AB_2107282; Millipore, Billerica, MA, USA). Subsequently, sections were washed and then incubated 3 h with a secondary antibodies cocktail of Cy3 donkey anti-rabbit (1:600; Jackson ImmunoResearch; #711-165-152, AB_2307443) and Cy2 donkey anti-chicken (1:400; Jackson ImmunoResearch; #703-225-155, AB_2340370). Slides were counterstained with DAPI for

5 min (1:20,000, Sigma Aldrich; #D21490), washed, dehydrated through an alcohol gradient and xylene, and sealed with DPX mounting medium (Slide mounting medium; Sigma-Aldrich; #06522).

Quantification of the density of nerve fibers on femoral periosteum and neuroma identification

For quantifications of $CGRP^+$ and $GAP43^+$ nerve fibers density, at least three sections of each mouse femur were analyzed. The areas with the highest density of nerve fibers at the metaphyseal periosteum were identified using a 10x objective. In all cases, these areas were located within 0.5 mm-1 mm distance from the distal femoral growth plate. Subsequently, a confocal image was obtained using the Z-stack function from a Carl Zeiss confocal microscope (model LSM 800, Jena, Germany). At least three images were obtained for each marker (20× magnification). The Z-stacked images were analyzed with ImageJ and nerve fibers were manually traced to determine their total length using the freehand line tool. Area of evaluation was manually determined tracing the area of the periosteum. This area was multiplied by the thickness of the section (25 um). Results were reported as the density of nerve fibers (total length) per volume of periosteum (mm^3) (17).

For the identification of neuroma-like structures, the following three criteria was followed 1) disordered mass of blind-ending axons ($CGRP^+$) that had an interlacing and/or whirling morphology, 2) structure with a size of more than 10 individual axons that is at least 20 µm thick and 70 µm long, and finally 3) a structure that is never observed in the periosteum of normal bone (57, 58).

Evaluation of human bone

Trephine iliac crest bone biopsies from newly diagnosed MM patients were collected at Sheffield Teaching Hospital upon informed consent and under approval from the East Midlands-Derby Research Ethics Committee, UK (REC19/YH/0319). Needle (3 mm) biopsies were collected under local lidocaine anaesthesia by a qualified medical practitioner as routine standard of care. Biopsies were formalin-fixed o/n, decalcified in formic acid, and paraffin embedded before sectioning at 3,5-µm thickness onto DAKO IHC Flex tissue slides (DAKO Aps, Glostrup, Denmark). Sections were deparaffinized in a xylene and alcohol gradient and subjected to antigen retrieval in Tris-EDTA buffer (pH 9.0) o/n. Slides were washed, blocked for endogenous peroxidases and blocked for unspecific

staining 20 min in 5% casein/TBS. Sections were labelled with a rabbit anti-PGP9.5 antibody (Sigma Aldrich, Søborg, Denmark; #SAB4503057, AB_10761291), detected with polymeric alkaline phosphatase conjugated anti-rabbit IgG (BrightVision DPVR-AP, Immunologic) and visualized with stay red (DAKO, Glostrup, Denmark). Next, sections were labelled with a mouse mAb against CD34 (Abcam, Cambridge, UK; #ab78165, AB_1566006), detected by polymeric horse radish peroxidase conjugated anti-mouse IgG (BrightVision DPVR-HRP, Immunologic) and visualized with deep space black (DSB, CCC). Sectioned were then blocked with mouse serum and labelled with a mouse mAb against CD138 (BD Pharmnigen, Allschwil, Switzerland; #552723, AB_394443), which was detected with horse radish peroxidase conjugated anti-fluorescein Fab fragments (Merck, Darmstadt, Germany) and visualized with diaminobenzidine (DAB^+; DAKO, Glostrup, Denmark). Finally, sections were counterstained with Mayer´s haematoxylin and mounted in Aquatex (Merck, Darmstadt, Germany). Slides were brightfield scanned with a 20x objective in an automated VS200 Slidescanner (Olympus Microscopy, Japan) and analysed in VS200 Desktop, (Olympus) by an experimenter blinded to the slide origin.

Mouse transcriptomics sequencing and analyses

In the transcriptomics experiment, 20 male C57BL/KaLwRijHsd mice underwent inoculation of 5TGM1-GFP cells or vehicle as described. Pain-like behaviours were assessed over time and mice were euthanized 24 days after surgery by transcardial perfusion with 10 ml of ice-cold PBS. Serum samples were collected and processed for IgG_{2b} assessment as described. Ipsilateral whole DRG lumbar L2-L4 were snap frozen in RNAse free Eppendorf tubes in a 3-Methylbutanol freezing bath. Tissue was homogenized in a bead miller and total RNA was extracted with a Qiagen RNAse microkit (Qiagen, Copenhagen, Denmark). RNA quality was assessed with an Agilent Bioanalyzer and samples with a RIN <8.0 were excluded (n=2).

Remaining samples underwent DNBSEQ transcriptome sequencing by BGI Denmark (BGI, Copenhagen, Denmark). Fastq files with reads with adaptors removed were further used in the bioinformatics analysis upon filtering out low quality ends. We used Salmon (version 1.5.2) (59) to

quantify transcript expression, using as reference the mouse cDNA set (coding and non-coding transcripts) corresponding to GRCm39. The salmon index was built using the corresponding GRCm39 genome as decoy sequence. Both the cDNA set and genome were obtained from Ensembl, release 104 (60, 61). Gene-level expression estimates were further obtained using the tximport R package (62). Genes with non-zero counts in at least 3 samples and with at least 10 estimated mapped reads in at least one of the samples were retained for further analysis. Differential expression analysis between the MM and sham was performed using the Wald test from DESeq2 R package (63).

Metastatic infiltration of MM cells within the DRG was assessed from the sequencing reads by counting the reads mapping to the eGFP, an artificial transfect to the 5TGM1 cell line. Bbduk (bbmap suite, v. 38.90 (64) with a kmer size of 31 was used to find the proportion of eGFP matching reads in each sample; eGFP sequences retrieved from (65).

GSEA (gene set enrichment analysis) for GO biological processes terms and reactome pathways was performed using the R packages clusterProfiler (66) and ReactomePA (67). Genes were ranked using the Wald test statistic (stat value) provided by DESeq2. We used the pairwise_termsim() function from enrichplot (68) to obtain the jaccard similarity coefficient (JC) in terms of overlapping gene sets between each two terms. Whenever JC was >0.7, we selected only the term with lowest adjusted p-value value in our enrichment results. Visualizations of the enrichment results were produced using the R packages DOSE (69) and enrichplot (68) and data is accessible in GEO under accession code GSE216802.

We compared our MM mouse data with DRG expression data from 6 other mouse models of painful conditions, as described in Bangash et al (26). The transcriptomes of DRGs from the test mice and their corresponding sham had been profiled using the Affymetrix GeneChip Mouse Transcriptome Array 1.0 and obtained from Additional file 3 (26). We compared our model with the 6 models in terms of overlap and direction of differentially expressed genes, as well as in terms of GSEA results. For our MM model we used the set of DEGs defined as padj<0.05, and for the models from Bangash et al, we used the sets of top 300 genes, sorted by pvalue. GSEA analysis for the six models was

performed as described for our MM transcriptomic data but ranking the genes by -log(pvalue)*(logFC/abs(logFC). For comparing GSEA results, we selected top 40 most enriched terms in the mouse MM model, sorted by absolute normalized enrichment score, and then extracted the values of the respective terms within the enrichment results corresponding to the other models.

Human transcriptomics sequencing and analyses

Human DRGs were collected from consenting cancer patients under ethical approval from UT Dallas (UTD) and MD Anderson Cancer Centre Institutional Review Boards. Tissue was extracted during thoracic vertebrectomy in patients presenting malignant spinal tumours; sequencing data from these patients has been previously published (30). Briefly, DRGs were extracted during spinal nerve root ligation and immediately transferred to cold sterile solution, cleaned and stored in dry ice until sequencing. RNA was extracted using TRIzol™ and cDNA was generated using an Illumina Tru-seq library preparation. Sequenced reads were then trimmed and same-length libraries (38bp) mapped to the GENCODE reference transcriptome (70), as previously described (30). Data were obtained from two DRGs belonging to one MM patient and 68 DRGs obtained from 39 patients; further information is compiled in Supplementary file S2. To evaluate gene expression profiles consistent with MM cell infiltration to the DRG, we first created a custom-made marker set from publicly available data. For this, we combined three high throughput datasets of MM cell gene expression based on different technologies: Affymetrix (31), bulk RNA-Seq (32) and single cell RNA-Seq (33), and one dataset measuring expression in normal human DRGs (34). For the Affymetrix (31) dataset, we obtained the processed data from the GEO NCBI portal using the GeoQuery R package (v.2.60.0) (71). We mapped the probesets of the HGU133Plus2 chip to Ensembl genes using the custom annotation provided by BrainArray (72). The file mapping probesets to Ensembl genes was obtained from the BrainArray download page, version 25 (brainarray.mbni.med.umich.edu). Probesets mapping to multiple genes were excluded and when multiple probesets corresponded to the same gene, the one with the highest mean average signal was selected. Probeset intensities were averaged across the 559 replicates, and in total, 16,554 Ensembl genes (of which 15,994 having the biotype “protein coding

genes") were uniquely mapped to probesets on the chip. We assigned ranks to genes by sorting them by decreasing average signal intensity. For the RNA-Seq dataset (32), we used the supplementary table with FPKM counts provided in the Gene Expression Omnibus (GEO) platform (study accession number GSE167968). We averaged expression levels across the 33 replicates and ranked genes by decreasing average FPKM units. For the single cell dataset (33), we used the supplementary file with transcripts per million (TPM) counts provided in GEO (GSE118900), and counted the number of cells (out of a total 597) in which each gene has a non-zero expression level. Normal DRG expression levels (34) were ranked by the decreasing average TPM counts across the three normal tissue samples. Combining the three MM transcriptomic datasets, we obtained a set of 2528 genes generally expressed in MM cells, i.e. ranked within the top 10,000 genes in both Affymetrix and bulk RNA-Seq and detected in at least 200 of the 597 cells of the single cell experiment. We further reduced this set to a subset of 40 genes by selecting those with an expression rank >15,000 (corresponding to <0.75 TPM) in normal DRG tissue.

We next interrogated MM cell infiltration in human DRG using the MM^{D24} mouse transcriptomic signature as a proxy. For this, we selected the set of upregulated DEGs with a p-adjusted <0.05 in MM^{D24} vs. $sham^{D24}$ mice and evaluated the behavior of their human orthologs in the DRG of MM patients compared to DRGs from patients with other cancer types. For each of the selected markers/DEGs, and for each cancer sample, we computed the percentile expression in relation to the other cancer samples.

Statistics

With exception of the transcriptomics experiments (see above), data were analysed and plotted using Graphpad Prism v.9.3.1 (GraphPad Inc., La Jolla, CA, USA), or SAS 9.4 (SAS Institute, Inc., Cary, NC, USA) and are presented as mean ± standard error of the mean (SEM). Group size was determined in G*Power v3.1.9.7 based on our previously published data (9) to detect a significant difference in limb use on post-surgical day 25 with a 90% power (α error prob. 0.05). Parametric data were

analysed by t-test, one-way ANOVA or repeated measures 2-way ANOVA with Bonferroni correction for multiple comparisons, as required. Non-parametric data was analysed by Friedman´s two-way test followed by Wilcoxon´s two-sample test for individual time-points. Transcriptomics data are available in supplementary data or publicly available in GEO (GSE216802); all other datasets are available in Supplementary File S4.

References

1. Kyle RA, Rajkumar SV. Criteria for diagnosis, staging, risk stratification and response assessment of multiple myeloma. Leukemia. 2009;23(1):3-9.
2. Kazandjian D, Landgren O, editors. A look backward and forward in the regulatory and treatment history of multiple myeloma: approval of novel-novel agents, new drug development, and longer patient survival. Seminars in oncology; 2016: Elsevier.
3. Kumar SK, Rajkumar SV, Dispenzieri A, Lacy MQ, Hayman SR, Buadi FK, et al. Improved survival in multiple myeloma and the impact of novel therapies. Blood. 2008;111(5):2516-20.
4. Ramsenthaler C, Kane P, Gao W, Siegert RJ, Edmonds PM, Schey SA, et al. Prevalence of symptoms in patients with multiple myeloma: a systematic review and meta-analysis. European journal of haematology. 2016;97(5):416-29.
5. Quinn B, Ludwig H, Bailey A, Khela K, Marongiu A, Carlson KB, et al. Physical, emotional and social pain communication by patients diagnosed and living with multiple myeloma. Pain management. 2022;12(1):59-74.
6. Coluzzi F, Rolke R, Mercadante S. Pain Management in Patients with Multiple Myeloma: An Update. Cancers. 2019;11(12):2037.
7. Niscola P, Scaramucci L, Romani C, Giovannini M, Tendas A, Brunetti G, et al. Pain management in multiple myeloma. Expert review of anticancer therapy. 2010;10(3):415-25.
8. Mercadante S. Treating breakthrough pain in oncology. Expert review of anticancer therapy. 2018;18(5):445-9.
9. Diaz-delCastillo M, Kamstrup D, Olsen RB, Hansen RB, Pembridge T, Simanskaite B, et al. Differential Pain-Related Behaviors and Bone Disease in Immunocompetent Mouse Models of Myeloma. JBMR Plus. 2020;4(2):e10252.
10. Diaz-delCastillo M, Kamstrup D, Olsen R, Hansen R, Pembridge T, Simanskaite B, et al. Differential pain-related behaviours and bone disease in immunocompetent mouse models of myeloma. JBMR Plus. 2019.
11. Mhaskar R, Kumar A, Miladinovic B, Djulbegovic B. Bisphosphonates in multiple myeloma: an updated network meta-analysis. The Cochrane database of systematic reviews. 2017;12:Cd003188.
12. Mach DB, Rogers SD, Sabino MC, Luger NM, Schwei MJ, Pomonis JD, et al. Origins of skeletal pain: sensory and sympathetic innervation of the mouse femur. Neuroscience. 2002;113(1):155-66.
13. Chartier SR, Mitchell SA, Majuta LA, Mantyh PW. The changing sensory and sympathetic innervation of the young, adult and aging mouse femur. Neuroscience. 2018;387:178-90.
14. Martin CD, Jimenez-Andrade JM, Ghilardi JR, Mantyh PW. Organization of a unique net-like meshwork of CGRP+ sensory fibers in the mouse periosteum: Implications for the generation and maintenance of bone fracture pain. Neuroscience Letters. 2007;427(3):148-52.
15. Mantyh PW. The neurobiology of skeletal pain. Eur J Neurosci. 2014;39(3):508-19.
16. Bloom AP, Jimenez-Andrade JM, Taylor RN, Castaneda-Corral G, Kaczmarska MJ, Freeman KT, et al. Breast cancer-induced bone remodeling, skeletal pain, and sprouting of sensory nerve fibers. J Pain. 2011;12(6):698-711.
17. Mantyh WG, Jimenez-Andrade JM, Stake JI, Bloom AP, Kaczmarska MJ, Taylor RN, et al. Blockade of nerve sprouting and neuroma formation markedly attenuates the development of late stage cancer pain. Neuroscience. 2010;171(2):588-98.
18. Sayilekshmy M, Hansen RB, Delaisse JM, Rolighed L, Andersen TL, Heegaard AM. Innervation is higher above Bone Remodeling Surfaces and in Cortical Pores in Human Bone: Lessons from patients with primary hyperparathyroidism. Sci Rep. 2019;9(1):5361.
19. Boyer NP, Gupton SL. Revisiting Netrin-1: One Who Guides (Axons). Front Cell Neurosci. 2018;12:221.
20. Madison RD, Zomorodi A, Robinson GA. Netrin-1 and peripheral nerve regeneration in the adult rat. Experimental neurology. 2000;161(2):563-70.
21. Dun X-P, Parkinson DB. Role of Netrin-1 Signaling in Nerve Regeneration. International Journal of Molecular Sciences. 2017;18(3):491.
22. Zhu S, Zhu J, Zhen G, Hu Y, An S, Li Y, et al. Subchondral bone osteoclasts induce sensory innervation and osteoarthritis pain. The Journal of clinical investigation. 2019;129(3):1076-93.

23. Wu CH, Yuan XC, Gao F, Li HP, Cao J, Liu YS, et al. Netrin-1 Contributes to Myelinated Afferent Fiber Sprouting and Neuropathic Pain. Mol Neurobiol. 2016;53(8):5640-51.
24. Jimenez-Andrade JM, Bloom AP, Stake JI, Mantyh WG, Taylor RN, Freeman KT, et al. Pathological sprouting of adult nociceptors in chronic prostate cancer-induced bone pain. Journal of Neuroscience. 2010;30(44):14649-56.
25. Ghilardi JR, Freeman KT, Jimenez-Andrade JM, Mantyh WG, Bloom AP, Kuskowski MA, et al. Administration of a tropomyosin receptor kinase inhibitor attenuates sarcoma-induced nerve sprouting, neuroma formation and bone cancer pain. Mol Pain. 2010;6:87.
26. Bangash MA, Alles SRA, Santana-Varela S, Millet Q, Sikandar S, de Clauser L, et al. Distinct transcriptional responses of mouse sensory neurons in models of human chronic pain conditions. Wellcome Open Res. 2018;3:78.
27. Inoue K, Tsuda M. Microglia in neuropathic pain: cellular and molecular mechanisms and therapeutic potential. Nat Rev Neurosci. 2018;19(3):138-52.
28. Chen G, Zhang Y-Q, Qadri YJ, Serhan CN, Ji R-R. Microglia in Pain: Detrimental and Protective Roles in Pathogenesis and Resolution of Pain. Neuron. 2018;100(6):1292-311.
29. Peters CM, Jimenez-Andrade JM, Kuskowski MA, Ghilardi JR, Mantyh PW. An evolving cellular pathology occurs in dorsal root ganglia, peripheral nerve and spinal cord following intravenous administration of paclitaxel in the rat. Brain Res. 2007;1168:46-59.
30. Ray PR, Shiers S, Caruso JP, Tavares-Ferreira D, Sankaranarayanan I, Uhelski ML, et al. RNA profiling of human dorsal root ganglia reveals sex-differences in mechanisms promoting neuropathic pain. Brain. 2022.
31. Barwick BG, Gupta VA, Matulis SM, Patton JC, Powell DR, Gu Y, et al. Chromatin Accessibility Identifies Regulatory Elements Predictive of Gene Expression and Disease Outcome in Multiple Myeloma. Clinical cancer research : an official journal of the American Association for Cancer Research. 2021;27(11):3178-89.
32. Zhan F, Huang Y, Colla S, Stewart JP, Hanamura I, Gupta S, et al. The molecular classification of multiple myeloma. Blood. 2006;108(6):2020-8.
33. Jang JS, Li Y, Mitra AK, Bi L, Abyzov A, van Wijnen AJ, et al. Molecular signatures of multiple myeloma progression through single cell RNA-Seq. Blood Cancer J. 2019;9(1):2.
34. Ray P, Torck A, Quigley L, Wangzhou A, Neiman M, Rao C, et al. Comparative transcriptome profiling of the human and mouse dorsal root ganglia: an RNA-seq-based resource for pain and sensory neuroscience research. Pain. 2018;159(7):1325-45.
35. Johnsen AT, Tholstrup D, Petersen MA, Pedersen L, Groenvold M. Health related quality of life in a nationally representative sample of haematological patients. European journal of haematology. 2009;83(2):139-48.
36. Olechnowicz SWZ, Weivoda MM, Lwin ST, Leung SK, Gooding S, Nador G, et al. Multiple myeloma increases nerve growth factor and other pain-related markers through interactions with the bone microenvironment. Scientific Reports. 2019;9(1):14189.
37. Hiasa M, Okui T, Allette YM, Ripsch MS, Sun-Wada GH, Wakabayashi H, et al. Bone pain induced by multiple myeloma is reduced by targeting V-ATPase and ASIC3. Cancer research. 2017;77(6):1283-95.
38. Sliepen SHJ, Diaz-Delcastillo M, Korioth J, Olsen RB, Appel CK, Christoph T, et al. Cancer-induced Bone Pain Impairs Burrowing Behaviour in Mouse and Rat. In vivo (Athens, Greece). 2019;33(4):1125-32.
39. Deacon RM. Burrowing in rodents: a sensitive method for detecting behavioral dysfunction. Nature protocols. 2006;1(1):118-21.
40. Porta-Sales J, Garzón-Rodríguez C, Llorens-Torromé S, Brunelli C, Pigni A, Caraceni A. Evidence on the analgesic role of bisphosphonates and denosumab in the treatment of pain due to bone metastases: A systematic review within the European Association for Palliative Care guidelines project. Palliative medicine. 2017;31(1):5-25.
41. Sopata M, Katz N, Carey W, Smith MD, Keller D, Verburg KM, et al. Efficacy and safety of tanezumab in the treatment of pain from bone metastases. Pain. 2015;156(9):1703-13.
42. Fahed D, Chettab A, Mathe D, Denis M, Traverse-Glehen A, Karlin L, et al. Netrin-1 expression and targeting in multiple myeloma. Leuk Lymphoma. 2022;63(2):395-403.
43. Diaz-delCastillo M, Hansen RB, Appel CK, Nielsen L, Nielsen SN, Karyniotakis K, et al. Modulation of Rat Cancer-Induced Bone Pain is Independent of Spinal Microglia Activity. Cancers. 2020;12(10):2740.

895 44. Honore P, Rogers SD, Schwei MJ, Salak-Johnson JL, Luger NM, Sabino MC, et al. Murine models of
896 inflammatory, neuropathic and cancer pain each generates a unique set of neurochemical changes in the
897 spinal cord and sensory neurons. Neuroscience. 2000;98(3):585-98.
898 45. Richardson PG, Delforge M, Beksac M, Wen P, Jongen JL, Sezer O, et al. Management of treatment-
899 emergent peripheral neuropathy in multiple myeloma. Leukemia. 2012;26(4):595-608.
900 46. Oortgiesen BE, Kroes JA, Scholtens P, Hoogland J, Dannenberg - de Keijzer P, Siemes C, et al. High
901 prevalence of peripheral neuropathy in multiple myeloma patients and the impact of vitamin D levels, a cross-
902 sectional study. Supportive Care in Cancer. 2022;30(1):271-8.
903 47. Dong M, Zhang J, Han X, He J, Zheng G, Cai Z. Baseline peripheral neuropathy was associated with age
904 and a prognostic factor in newly diagnosed multiple myeloma patients. Scientific Reports. 2022;12(1):10061.
905 48. Dickenman RC, Chason JL. Alterations in the dorsal root ganglia and adjacent nerves in the leukemias,
906 the lymphomas and multiple myeloma. Am J Pathol. 1958;34(2):349-61.
907 49. Lawson MA, Paton-Hough JM, Evans HR, Walker RE, Harris W, Ratnabalan D, et al. NOD/SCID-GAMMA
908 mice are an ideal strain to assess the efficacy of therapeutic agents used in the treatment of myeloma bone
909 disease. PLoS One. 2015;10(3):e0119546.
910 50. Bouxsein ML, Boyd SK, Christiansen BA, Guldberg RE, Jepsen KJ, Müller R. Guidelines for assessment of
911 bone microstructure in rodents using micro-computed tomography. Journal of bone and mineral research :
912 the official journal of the American Society for Bone and Mineral Research. 2010;25(7):1468-86.
913 51. Peters CM, Ghilardi JR, Keyser CP, Kubota K, Lindsay TH, Luger NM, et al. Tumor-induced injury of
914 primary afferent sensory nerve fibers in bone cancer pain. Exp Neurol. 2005;193(1):85-100.
915 52. Glaser J, Gonzalez R, Perreau VM, Cotman CW, Keirstead HS. Neutralization of the chemokine CXCL10
916 enhances tissue sparing and angiogenesis following spinal cord injury. J Neurosci Res. 2004;77(5):701-8.
917 53. Ireland WP, Fletcher TF, Bingham C. Quantification of microvasculature in the canine spinal cord. The
918 Anatomical record. 1981;200(1):102-13.
919 54. Jimenez-Andrade JM, Herrera MB, Ghilardi JR, Vardanyan M, Melemedjian OK, Mantyh PW.
920 Vascularization of the dorsal root ganglia and peripheral nerve of the mouse: implications for chemical-
921 induced peripheral sensory neuropathies. Mol Pain. 2008;4:10.
922 55. Weidner N, Semple JP, Welch WR, Folkman J. Tumor angiogenesis and metastasis--correlation in invasive
923 breast carcinoma. N Engl J Med. 1991;324(1):1-8.
924 56. Hirakawa H, Okajima S, Nagaoka T, Kubo T, Takamatsu T, Oyamada M. Regional differences in blood-
925 nerve barrier function and tight-junction protein expression within the rat dorsal root ganglion. Neuroreport.
926 2004;15(3):405-8.
927 57. Devor M, Wall PD. Type of sensory nerve fibre sprouting to form a neuroma. Nature.
928 1976;262(5570):705-8.
929 58. Sung JH, Mastri AR. Aberrant peripheral nerves and microneuromas in otherwise normal medullas. J
930 Neuropathol Exp Neurol. 1983;42(5):522-8.
931 59. Patro R, Duggal G, Love MI, Irizarry RA, Kingsford C. Salmon provides fast and bias-aware quantification
932 of transcript expression. Nature Methods. 2017;14(4):417-9.
933 60. Howe KL, Achuthan P, Allen J, Allen J, Alvarez-Jarreta J, Amode MR, et al. Ensembl 2021. Nucleic Acids
934 Research. 2020;49(D1):D884-D91.
935 61. Cunningham F, Allen JE, Allen J, Alvarez-Jarreta J, Amode M R, Armean Irina M, et al. Ensembl 2022.
936 Nucleic Acids Research. 2021;50(D1):D988-D95.
937 62. Soneson C, Love MI, Robinson MD. Differential analyses for RNA-seq: transcript-level estimates improve
938 gene-level inferences. F1000Res. 2015;4:1521.
939 63. Love MI, Huber W, Anders S. Moderated estimation of fold change and dispersion for RNA-seq data with
940 DESeq2. Genome Biol. 2014;15(12):550.
941 64. Bushnell B. BBMAP. https://sourceforge.net/projects/bbmap/: SourceForge.
942 65. SnapGene. Dotmatics [
943 66. Sacks D, Baxter B, Campbell BCV, Carpenter JS, Cognard C, Dippel D, et al. Multisociety Consensus Quality
944 Improvement Revised Consensus Statement for Endovascular Therapy of Acute Ischemic Stroke. Int J Stroke.
945 2018;13(6):612-32.
946 67. Yu G, He QY. ReactomePA: an R/Bioconductor package for reactome pathway analysis and visualization.
947 Mol Biosyst. 2016;12(2):477-9.

948 68. Yu G. Enrichplot: visualization of functional enrichment result. R package version. 2019;1(2).
949 69. Yu G, Wang LG, Yan GR, He QY. DOSE: an R/Bioconductor package for disease ontology semantic and
950 enrichment analysis. Bioinformatics. 2015;31(4):608-9.
951 70. Frankish A, Diekhans M, Ferreira A-M, Johnson R, Jungreis I, Loveland J, et al. GENCODE reference
952 annotation for the human and mouse genomes. Nucleic acids research. 2019;47(D1):D766-D73.
953 71. Davis S, Meltzer PS. GEOquery: a bridge between the Gene Expression Omnibus (GEO) and
954 BioConductor. Bioinformatics. 2007;23(14):1846-7.
955 72. Dai M, Wang P, Boyd AD, Kostov G, Athey B, Jones EG, et al. Evolving gene/transcript definitions
956 significantly alter the interpretation of GeneChip data. Nucleic Acids Research. 2005;33(20):e175-e.
957 73. Watson C, Paxinos G, Kayalioglu G, Heise C. Chapter 16 - Atlas of the Mouse Spinal Cord. In: Watson C,
958 Paxinos G, Kayalioglu G, editors. The Spinal Cord. San Diego: Academic Press; 2009. p. 308-79.
959 74. Diaz-delCastillo M, Christiansen SH, Appel CK, Falk S, Woldbye DPD, Heegaard A-M. Neuropeptide Y is
960 Up-regulated and Induces Antinociception in Cancer-induced Bone Pain. Neuroscience. 2018;384:111-9.
961 75. Ansari N, Müller S, Stelzer EHK, Pampaloni F. Chapter 13 - Quantitative 3D Cell-Based Assay Performed
962 with Cellular Spheroids and Fluorescence Microscopy. In: Conn PM, editor. Methods in Cell Biology. 113:
963 Academic Press; 2013. p. 295-309.

964

965

SUPPLEMENTARY METHODS

Locomotor activity

Distance and speed moved by freely walking mice was automatically measured with Ethovision XT 8.5 (Noldus Information Technology, Wageningen, The Netherlands). On post-surgical day 24, myeloma-bearing and sham mice were individually placed in standard, transparent plastic cages (125 x 266 x 185 mm) in a quiet, dimly illuminated room and their free movement was tracked in 1 min time-beans over a total of 15 minutes.

Spinal cord tissue evaluation

Spinal cords were serially sectioned at 30-µm thickness; lumbar regions L1 to L6 were identified as per their described grey matter anatomy (73) and collected. Slides were washed in PBS, permeabilized in 0,1% triton X in PBS and blocked with 2% BSA (Sigma Aldrich, Søborg, Denmark). Then, slides were o/n incubated with a rabbit antibody against Iba-1 (Wako Pure Chemical Industries, Ltd., Neuss, Germany), GFAP (DAKO Agilent, Glostrup, Denmark) or P-p38 (Thr180/Tyr182) (Bionordika, Cell Signaling Technology, Herlev, Denmark) at 4°C. Labelling was detected with an Alexa Fluor 594 goat anti-rabbit secondary antibody or Alexa Fluor 594 donkey anti-rabbit (1:300, Invitrogen, Themo Fisher Scientific, Slangerup Denmark). Slides were then washed, counterstained with DAPI (Themo Fisher Scientific, Slangerup Denmark) and mounted with Fluorescent Mounting Medium (DAKO Agilent, Glostrup, Denmark). Negative controls were performed by omission of primary antibody. Serial sections separated by at least 240 µm were imaged with a 20x objective using a Zeiss Axioskop 2 microscope with a high resolution Axiocam MRm camera (HAL100; Zeiss, Feldbach, Switzerland) and a fluorescent transmitter (HXP 120, Digital Scientific, Cambridge, UK). Pseudo-anonymised images were analysed in Image J (National Institutes of Health, NIH, Bethesda, USA) by a researcher blinded to experimental mouse and group. Briefly, positive Iba-1 and P-p38 cells were quantified within a pre-determined area of interest (347 x 260 μm^2) located in the dorsal horn and including laminae I-IV. GFAP was quantified by measuring fluorescence intensity in the

dorsal horn and calculating the corrected total cell fluorescence (CTCF) as previously described by us and others (74, 75).

Supplementary Table S1

	Procedure description
Randomization	• Time-course experiment: mice were randomized into sham or MM according to their baseline burrowing performance and baseline weight. • Transcriptomics experiment: mice were randomized into sham or MM according to weight. Randomization was performed by listing all mice from lower to higher baseline burrowing capacity or weight and stratifying in two groups. Average baseline burrowing capacity or weight was then calculated and mice were inter-exchanged among groups until the averages were equal ± 10%.
Allocation concealment	To minimize bias and cage, mice from different groups (i.e. MM and sham) were caged together. No physical distinctions among groups were available at mouse or cage level. The allocation code was kept in a close, secure file until the end of the experiment.
Blinding	All behavioural experiments were conducted by an investigator blinded to the experimental group.
Exclusion criteria	• In all experiments: mice displaying surgical complications. • In the time-course experiment: 10% worst burrowers (excluded only from burrowing behaviour). • In the transcriptomics experiment: mice with RNA RIN < 8.0

Reporting of excluded animals	• Time-course experiment:
	  • 2 mice due to surgical complications.
	  • 10 mice due to cancer contamination in vehicle solution.
	  • 2 mice in burrowing behaviour (10% worst burrowers)
	• Transcriptomics: 2 mice due to low quality RNA.

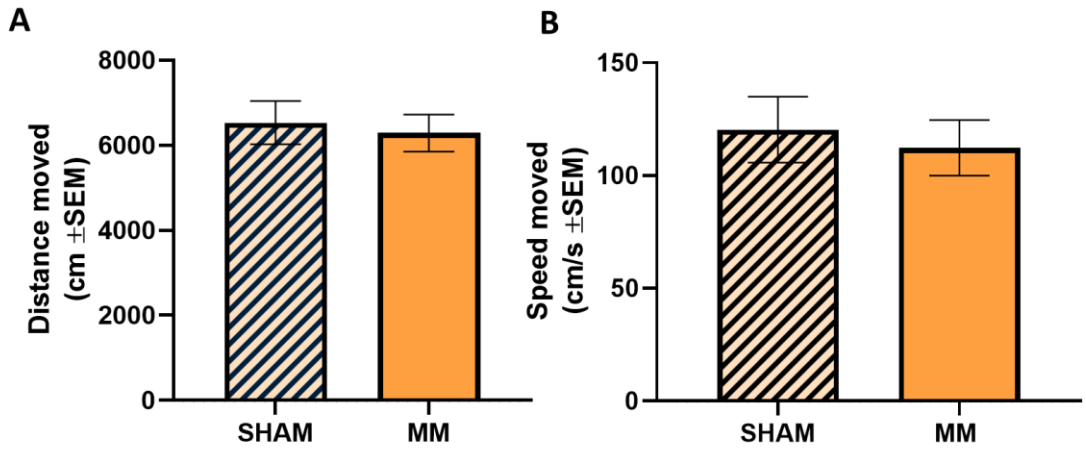

Supplementary Figure S1. The mobility of myeloma-bearing mice was unaffected by disease progression. On post-surgical day 26, distance moved (A) and speed moved (B) on MM mice and sham was not significantly different, indicating that the MIBP deficits in the limb use score were not cause by motor impairment. Data are presented as mean ± SEM. Sham n=4; MM n=10.

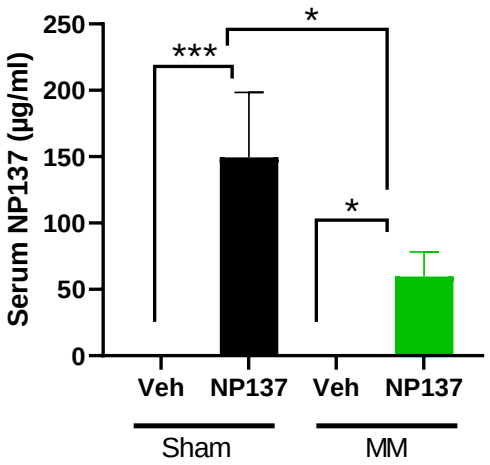

Supplementary Figure S2. Serum levels of NP137.. The serum levels of sham drug-treated mice were higher than those of MM drug-treated mice; increased antibody clearance and volume distribution is often seen in cancer models, where antibody pharmacokinetics change in parallel to tumour size. Data are presented as mean ± SEM. Sham n=4; MM n=8/9.

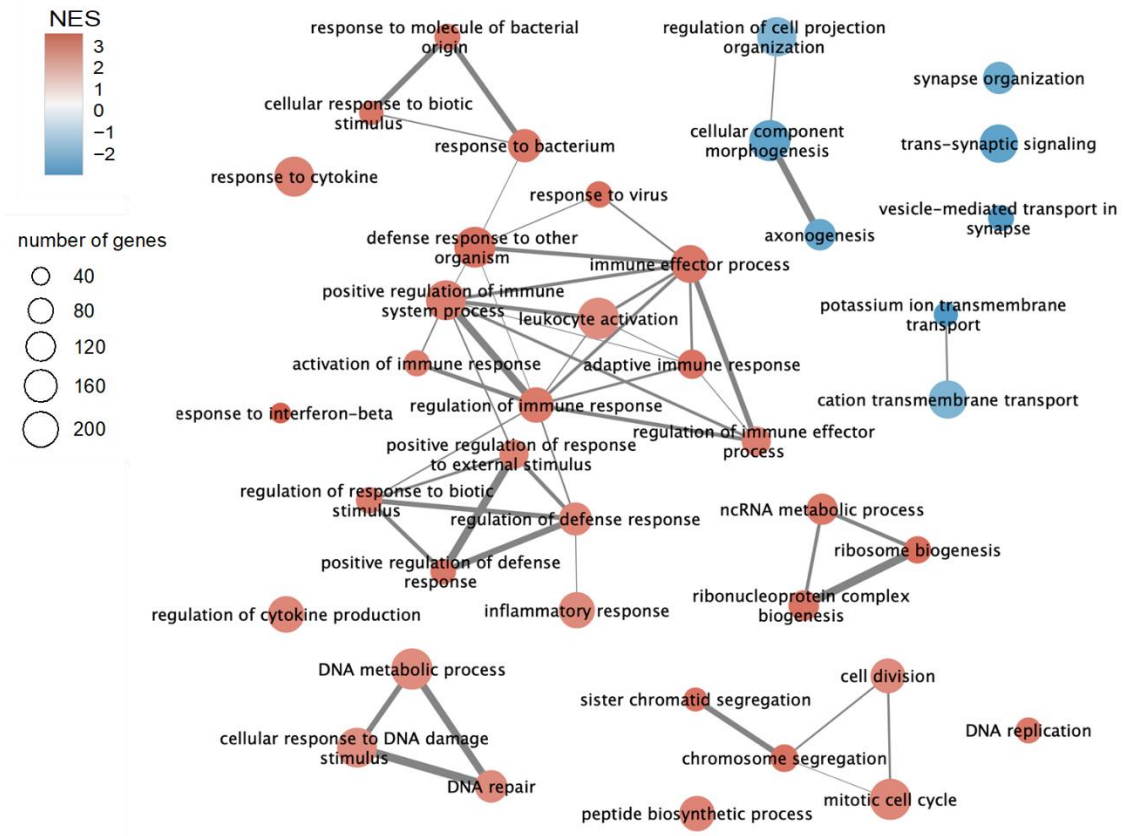

Supplementary Figure S3. Top 40 GO BP terms from GSEA analyses. Network view after filtering out highly similar terms. Node color represents the normalized enrichment score (NES) (red – positive, corresponding to upregulated terms and blue negative – downregulated terms). Node size is proportional to the number of genes associated to the term. Edges represent the JC between each two terms. Edge width is proportional with JC; only edges with JC>0.3 are shown. The main upregulated terms are related to immune response, cell cycle and DNA repair, while the downregulated terms are related to neuronal signaling.

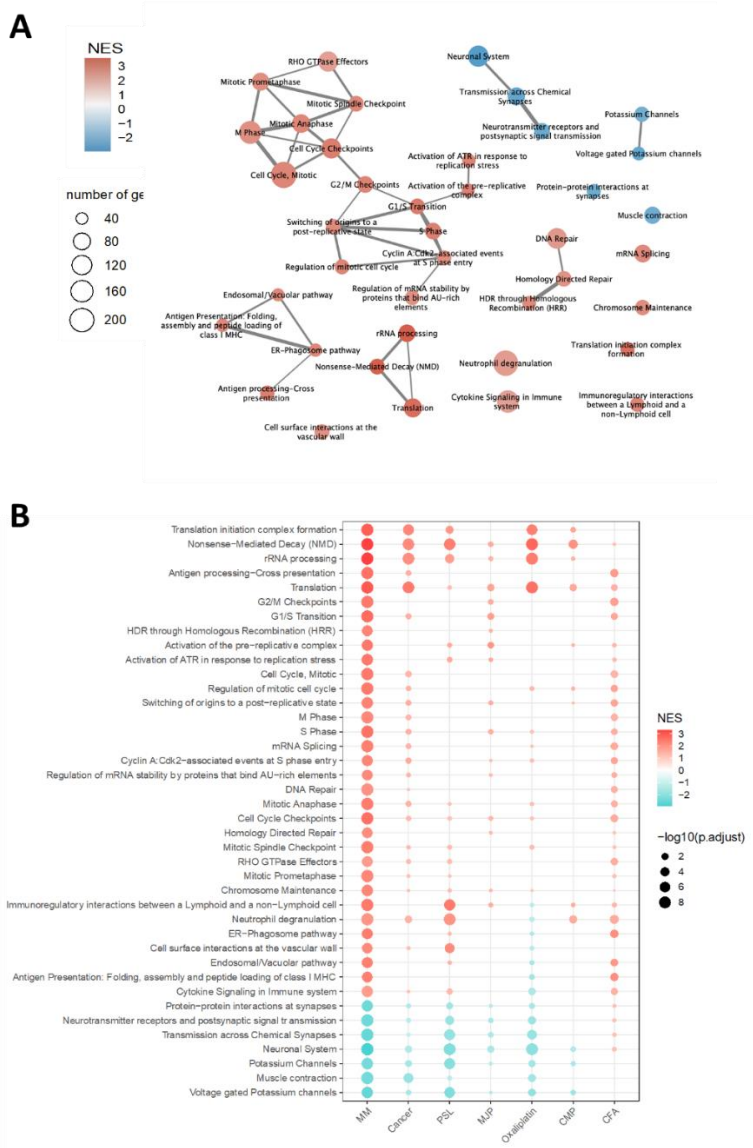

Supplementary Figure S4. A. **Network view of the top 40 enriched Reactome pathways from GSEA analysis.** Node color represents the normalized enrichment score (NES) (red – positive, corresponding to upregulated pathways and blue – negative, downregulated pathways). Node size is proportional to the number of genes associated to the term. Edges represent the JC between each two terms. Edge width is proportional with JC; only edges with JC>0.3 are shown. Most upregulated pathways are related to cell cycle, checkpoints, DNA repair, and downregulated pathways are related to neuronal signaling. **B.** Comparison of MIBP and the 6 models from Bangash et.al. in terms of GSEA for Reactome pathways. Normalized enrichment scores (NES) and corresponding adjusted p-values, for the top 40 enriched Reactome pathways in MIBP, are visualized across all seven pain models.

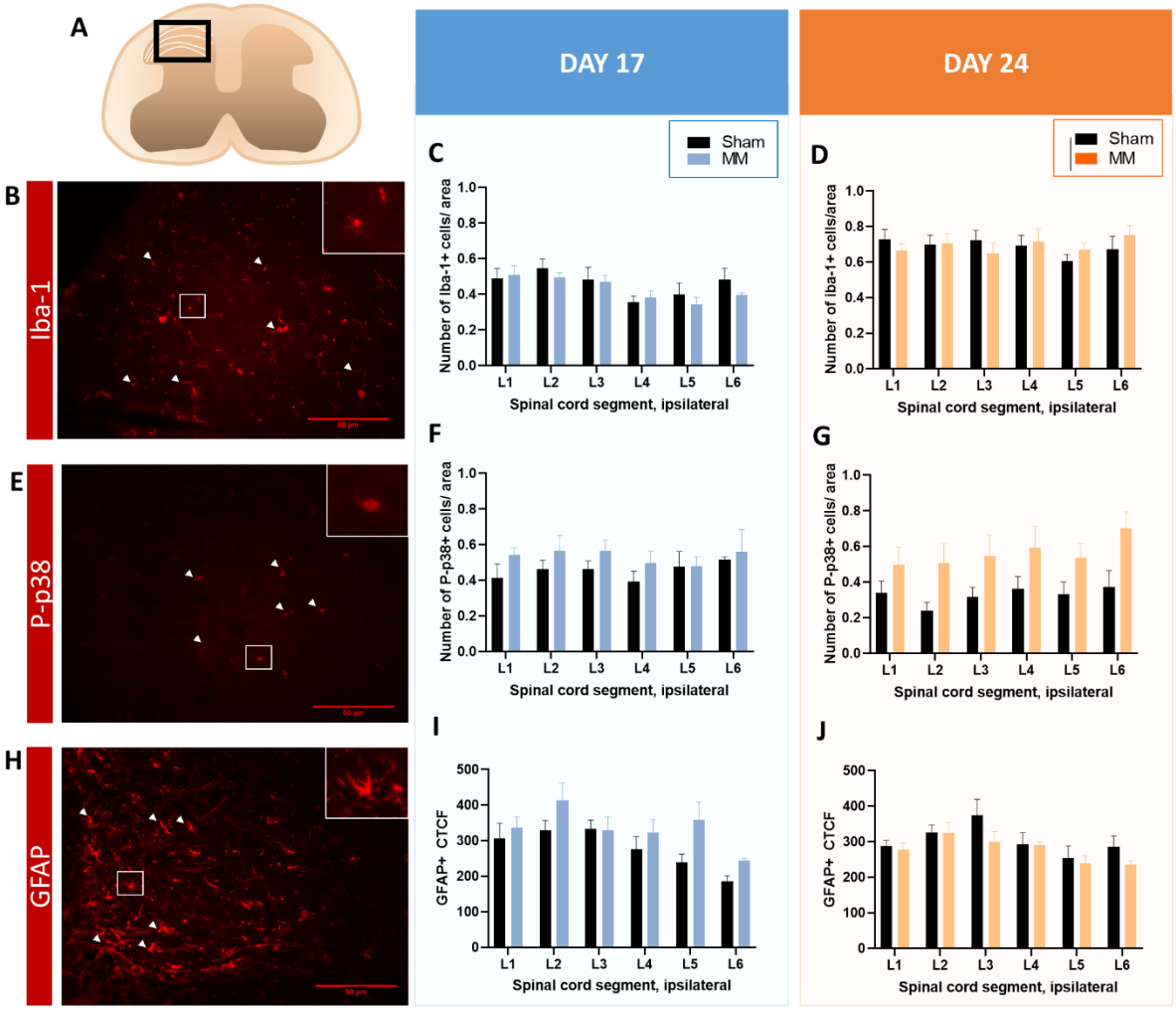

Supplementary Figure S5. Microglia reaction and astrocytosis are not a main feature of MIBP. (A) Overview of the 347 x 260 µm2 area encompassing laminae I-IV of the dorsal horn in which Iba-1, Pp38 and GFAP were analysed. (B, E, H) Representative image of Iba1^{+} microglia cells (B), Pp38^{+} microglia cells (E) or GFAP^{+} astrocytes (H) in the ipsilateral dorsal horn of the spinal cord (white arrowheads). (C, D, F, G) The relative number of Iba-1^{+} (C, D) or P-p38 (F, G) microglia cells in the ipsilateral dorsal horn of the spinal cord of lumbar regions L1 to L6 was unchanged between MM and sham mice euthanized on day 17 or 24. (I, J) The level of normalized GFAP expression in the dorsal horn of the spinal cord was similar between MM and sham mice euthanized on post-surgical day 17 or 24. L=lumbar. Data are presented as mean ± SEM. Sham n=6-8; MM n=7-8.